Impact of Prussian Blue Particle Size Distribution on Electrochemical Performance of Gel Polymer ElectrolyteBased NaIon Cells

ChemElectroChem

Research Article
doi.org/10.1002/celc.202400350

Chemistry Europe
European Chemical Societies Publishing

www.chemelectrochem.org

Impact of Prussian Blue Particle Size Distribution on Electrochemical Performance of Gel Polymer Electrolyte-Based Na-Ion Cells

Asia Patriarchi,[a] Jonathan Caroni,[b] Luca Minnetti,[a] Leonardo Sbrascini,[a] Hamideh Darjazi,[c, d] Francesco Nobili,[a, d] and Miguel Ángel Muñoz-Márquez*[a, d]

Lithium-ion batteries (LIBs) are one of the most advanced electrochemical energy storage technologies. However, the increasing demand for LIBs, coupled with problems related to availability and lack of manufacturing centers, has led to lithium market inflation. At this point, sodium-ion batteries (SIB) represent an economically and environmentally attractive alternative for LIBs. Prussian Blue cathodes (PB) have been extensively studied as cost-effective materials with volumetric variations that allow the accommodation of sodium ions in the structure. Herein, we present a quasi-solid Na-ion cell based on PB cathode and green gel polymer electrolyte (GPE). Nanometric and micrometric PB powders are synthesized and characterized using a wide variety of structural, compositional and electrochemical techniques. The effect of the PB particle size in combination with different electrolytes is investigated. Enhanced cell safety is obtained using a GPE prepared by following a novel green method that avoids using toxic organic solvents. All the tested cells report remarkable electrochemical performance, being the nanometric-PB/ GPE/ Na cell configuration the one with the highest specific capacity and almost no capacity loss after 100 cycles, outperforming analogous cells assembled with liquid electrolyte. This electrochemical stability is triggered by a robust electrode-electrolyte interphase.

Introduction

Nowadays, there is an urgent need to explore green and sustainable energy sources and storage systems. The growing energy demand has pushed the fossil fuel use ultimately leading to escalating levels of air pollution and greenhouse gas emissions.[1–3] Lithium-ion batteries (LIBs) have become very successful energy storage systems thanks to their outstanding properties, such as high energy density, good cyclability and long cycle life. These have allowed their application in fields like portable electronics, energy storage and electric vehicles.[4–7] However, lithium cost and availability are under question since it is mainly located in restricted areas of the world and its extraction raises economic, social, and environmental concerns. For instance, lithium mining risks of air and water contamination by chemicals and heavy metals, could result in a long-term ecological damage.[8–10] For all the reasons above, sodium ion batteries (SIBs) are a promising alternative to LIBs due to the abundant and homogeneous distribution of sodium in the Earth's crust, becoming an almost inexhaustible resource. Additionally, SIBs are economically and environmentally attractive,[11] even if their use is still hindered by the lack of stable electrode materials capable of undergoing significant volumetric changes that accommodate suitable amounts of sodium ions. Thus, it is worth noting that considerable research has recently been devoted to identifying cost-effective hosts for sodium insertion with both high specific capacity and extended cycle life;[12–14] commonly used sodium cathode materials include $NaMnO_2$ and Nasicon-type materials[12,13] but, among all, Prussian Blue (PB) and its analogues (PBA)[14–16] are of particular interest thanks to their metal-organic framework-type structure characterized by the intrinsic presence of Fe^{2+}/Fe^{3+} redox couple at the vertices and CN bridges that originates an ordered interconnected cubic structure.[16] This type of synthetic compound was first reported in the 18th century[17] and they have been extensively studied as cost-effective cathode for sodium ion batteries, since they show a reversible phase transition during sodium insertion/extraction process, an easy synthetic pathway and high specific capacity (170 mAh g^{-1}).[14,18]

However, as previously occurred with LIBs, the large-scale use of SIBs faces practical challenges: the use of conventional liquid electrolytes not only raises safety concerns but also lacks structural consistency, hence requiring the use of separators

[a] A. Patriarchi, L. Minnetti, Dr. L. Sbrascini, Dr. F. Nobili, Dr. M. Á. Muñoz-Márquez
School of Science and Technology; Chemistry division, University of Camerino, Via Madonna delle Carceri- ChIP, Camerino(MC) 62032, Italy
E-mail: miguel.munoz@unicam.it

[b] J. Caroni
Department of Chemistry, Biology and Biotechnologies, University of Perugia, Via Elce di Sotto 8, Perugia (PG) 06123, Italy

[c] Dr. H. Darjazi
GAME Lab, Department of Applied Science and Technology (DISAT), Politecnico di Torino, C.so Duca degli Abruzzi 24, Torino (TO) 10129, Italy

[d] Dr. H. Darjazi, Dr. F. Nobili, Dr. M. Á. Muñoz-Márquez
National Reference Center for Electrochemical Energy Storage (GISEL), Via Giusti 9, Firenze (FI) 50121, Italy.

Supporting information for this article is available on the WWW under https://doi.org/10.1002/celc.202400350

that, increase the total weight of the battery while reducing the cell energy density.[19] Ideally, an optimal electrolyte should be affordable, safe and good ionic conductor:[20] gel polymer electrolytes (GPEs) meet these requirements and emerge as a promising candidate for the substitution of conventional liquid electrolytes in sodium-ion batteries. In general, GPEs are made by one or more polymers that create a lattice in which charge carriers could be trapped. These electrolytes enhance safety and minimize leakage risk while delivering high conductivity even at room temperature.[11,20] In addition, this type of electrolyte is well suited for SIBs due to the flexibility of the polymer that can accommodate significant volumetric variations and handle changes in electrode size, such as the ones occurring during the charge and discharge processes of the cells.

In this work, two Prussian Blue cathode materials were synthesized using a single source of iron, different size distributions were obtained by varying the stirring time of the reaction. Two cathode materials were obtained in terms of particle size: one submicrometric that we called nanometric Prussian Blue (NPB) and one micrometric Prussian Blue (MPB). The materials were extensively characterized by means of X-Ray powder diffraction (XRPD), scanning electron microscopy (SEM), Thermal gravimetric analysis (TGA), Fourier-Transform infrared (FTIR) and Raman spectroscopy together with electrochemical techniques such as potentiostatic electrochemical impedance spectroscopy (PEIS), cyclic voltammetry (CV), linear sweep voltammetry (LSV) and galvanostatic cycling with potential limitation (GCPL). The electrochemical performances of NPB and MPB were assessed in terms of the particle size using two different electrolytes: a conventional liquid electrolyte and the new PEO/PVDF-based GPE that was synthesized and fully characterized. The results revealed remarkable performances for NPB and MPB with both the electrolytes, but the NPB/GPE/Na cell configuration achieved the highest specific capacity and virtually no capacity loss was detected over 100 charge-discharge cycles, as confirmed by PEIS measurements, where a more stable interfacial behavior seems to be promoted, outperforming its analogue cell with liquid electrolyte cell and all MPB-based cells.

Results and Discussion

Prussian Blue Cathodes

Figures 1a–b show SEM images from NPB and MPB materials respectively. For both samples, a well-defined cubic shape was obtained, as best illustrated in the inset where the magnification of a single cube is reported. The SEM analysis revealed a well-developed particle morphology, overall, the particles appeared to be well separated and with a smooth surface, with only a small portion showing minor imperfections such as a slight dulling of the edges probably due to zeolitic water competing with sodium for the occupation of the interstices of the Prussian structure.[21] However, it is worth saying that removing all the crystal water can be a challenging process, especially as the reaction environment is aqueous and defects due to the presence of coordinated water molecules are often unavoidable.[22]

Furthermore, for NPB, a homogeneous size distribution is estimated, with a mean value of around 700 nm (Figure S1); instead, MPB, has a broader particle size distribution with particles ranging from 800 to 1600 nm (Figure S1), with a slight agglomeration of the individual cubes into larger clusters, probably due to a fast nucleation mechanism. An EDS analysis was conducted to evaluate the purity of the two materials and the mapping confirmed a uniform distribution of elements (see Figure S2 and S3). As only carbon, oxygen, nitrogen, iron and sodium were detected, it is safe to assume that there are no contaminations or impurities.

Moreover, EDX analysis was performed on NPB and MPB to gather information that could help on determining the stoichiometric composition of the materials. The EDX results are presented in Table 1.

Table 1 shows that the atomic composition of NPB and MPB are very similar to each other. In particular, the carbon to nitrogen ratio is approximately 1:1, which agrees with the presence of the CN groups in the structure. It is worth noting that the slight excess of carbon detected may be due to the composition of the sample holder used for the SEM analysis,

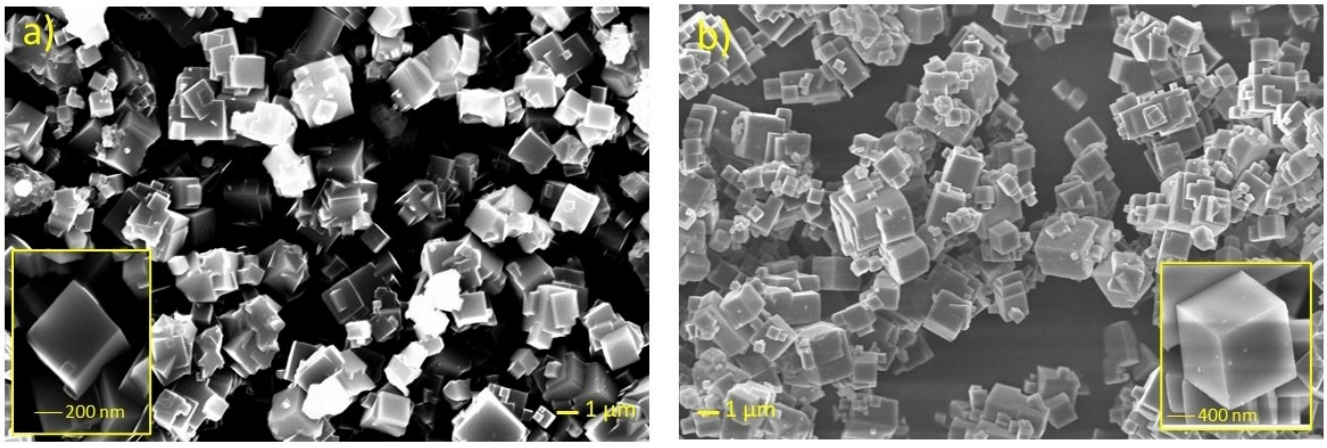

Figure 1. (a) SEM overview image of NPB (EHT = 25.00 kV), with a detailed view of a single cube provided in the inset (b) MPB SEM overview image (EHT = 25.00 kV) and magnification of the single cube in the inset.

Table 1. EDX values obtained from SEM analysis of NPB and MPB.

Element	NPB (at.%)	MPB (at.%)
Carbon	35.3	34.7
Nitrogen	31.6	31.0
Iron	12.8	9.3
Sodium	2.2	2.3
Oxygen	18.1	22.7

rather than the sample itself. Furthermore, the nitrogen to iron ratio of approximately 3:1 confirms the appropriate molar ratio of iron to cyanide groups and the nitrogen to sodium ratio allows estimation of the amount of Na incorporated into the structure. MPB exhibited a slight increase in sodium content, which may be attributed to the longer reaction time. Therefore, NPB and MPB's composition is estimated to be $Na_{0.4}Fe[Fe(CN)_6]$ and $Na_{0.5}Fe[Fe(CN)_6]$ respectively.

In addition, the two samples were analyzed by CHN elemental analysis to determine the carbon and nitrogen content more accurately and confirm the atomic percentages obtained by SEM (Figure S4). The results of both techniques are consistent, supporting the SEM estimation. The atomic percentages obtained by elemental analysis are reported in Table 2.

Moreover, to determine the zeolitic and adsorbed water content in both NPB and MPB, the samples were further investigated by means of TGA, as shown in Figure S5. To quantify the weight loss relative to water, NPB and MPB were treated under a nitrogen atmosphere at a heating rate of 10 °C/minute from 30 °C to 350 °C. The micrometric cathode exhibited a greater weight loss (12%) compared to the sub-nanometric one (9%), likely attributed to a higher water content, as previously suggested by EDX and CHN elemental analysis where higher atomic percentages of oxygen and hydrogen were detected.

In addition, to further investigate the sodium-to-iron ratio and confirm the stoichiometry of the two compounds, an inductively coupled plasma (ICP) analysis was conducted (see Table S1).

Figures 2a and 2b display the X-ray powder diffraction (XRPD) patterns of the two Prussian Blue samples. The diffractograms were fitted using WinPlotr-2006 software, and the Miller indexes of the planes were reported. Qualitative phase analysis was performed for both samples by applying a search and match procedure with the help of the PANalytical X'Pert Highscore program and the Crystallography Open Database (COD). The results indicate the presence of the $Fe_4(Fe(CN)_6)_3(H_2O)_{14}$ phase in both samples.[23] Moreover, the unit cell parameters were determined by means of Treor90 and Dicvol06 programs after fitting the diffraction patterns using WinPlotr-2006 software, where the position of the maxima was determined by fitting the Kα1 and the Kα2 contributions for every peak with a pseudo-Voigt function. Both calculation programs converged with a satisfactory figure of merit, giving a cubic crystal system. Among the most probable space groups of the material, Fm-3 m was selected as result of Chekcell analysis and thus confirmed by previous works.[24–27]

Table 2. C, H and N atomic percentage in both NPB and MPB obtained by elemental CHN analysis.

Element	MPB (at.%)	NPB (at.%)
C	21.1	21.7
H	1.9	1.3
N	23.1	24.6

The Rietveld refinement through GSAS-II was executed to optimize and confirm the previously calculated cell parameters data for NPB and MPB. Global parameters, such as sample displacement, scale factors and background, were first refined followed by structural parameters, such as isothermal parameters, atomic coordinates, and site occupancies. It is worth noting that the correction for the preferred orientation along the [h 0 0] direction was also included in the refinement. The obtained patterns are shown in Figures 2c and 2d, together with the atomic positions and their fractional occupancy in Table S2 and Table S3, respectively.

The crystal structures obtained are in good agreement with those reported in the literature,[23] only with slight differences due to the presence of sodium atoms that occupy some tetrahedral sites in the cubic structure of Prussian blue samples, in particular length axes change from 10.15 to 10.19 Å and the cell volume from 1047 to 1060 $Å^3$. In addition, the size and strain values of the crystalline domains were obtained from the refinement, confirming a larger average size of the crystallites for MPB (909 nm) than those of NPB sample (550 nm) which is in good agreement with the particle size estimation made from SEM analysis. Furthermore, similar strain values for both MPB and NPB were found which turn out to be of 0.3% and 0.4% respectively, as shown in Table 3.

A graphical representation of the calculated Prussian blue structure is reported in Figure 2e.

A deeper investigation of NPB and MPB was carried out using Raman spectroscopy analyzing both the powders and the pristine electrodes, as shown in Figure S6 a,b. All the expected PB Raman features were detected for both NPB and MPB, and the characteristic bands have been highlighted in different colors on the spectra in order to aid their identification (see Figure S6 a,b). Previous reports assign two cyanide stretching peaks in the 2170 cm^{-1} and 2040 cm^{-1} interval, being their position strongly influenced by the valence state of binding iron.[28–30] Consistently, in this work, there is a fairly intense band at around 2150 cm^{-1} and a weaker peak at 2100 cm^{-1} (framed in yellow, Figure S6), which may be attributed to the stretching of CN bonded with Fe(II) and Fe(III).[31] Moreover, the Fe–C stretching band (framed in green, Figure S6) could be detected around 550 cm^{-1}, instead, Fe–CN–Fe stretching deformation (framed in blue, Figure S6) appears at 250 cm^{-1}.[31] Besides the expected Raman peaks, the pristine electrode exhibited two additional peaks (highlighted in orange, Figure S6) related to the D (1314 cm^{-1}) and G (1598 cm^{-1}) bands of conductive carbon used in the electrode formulation.[32]

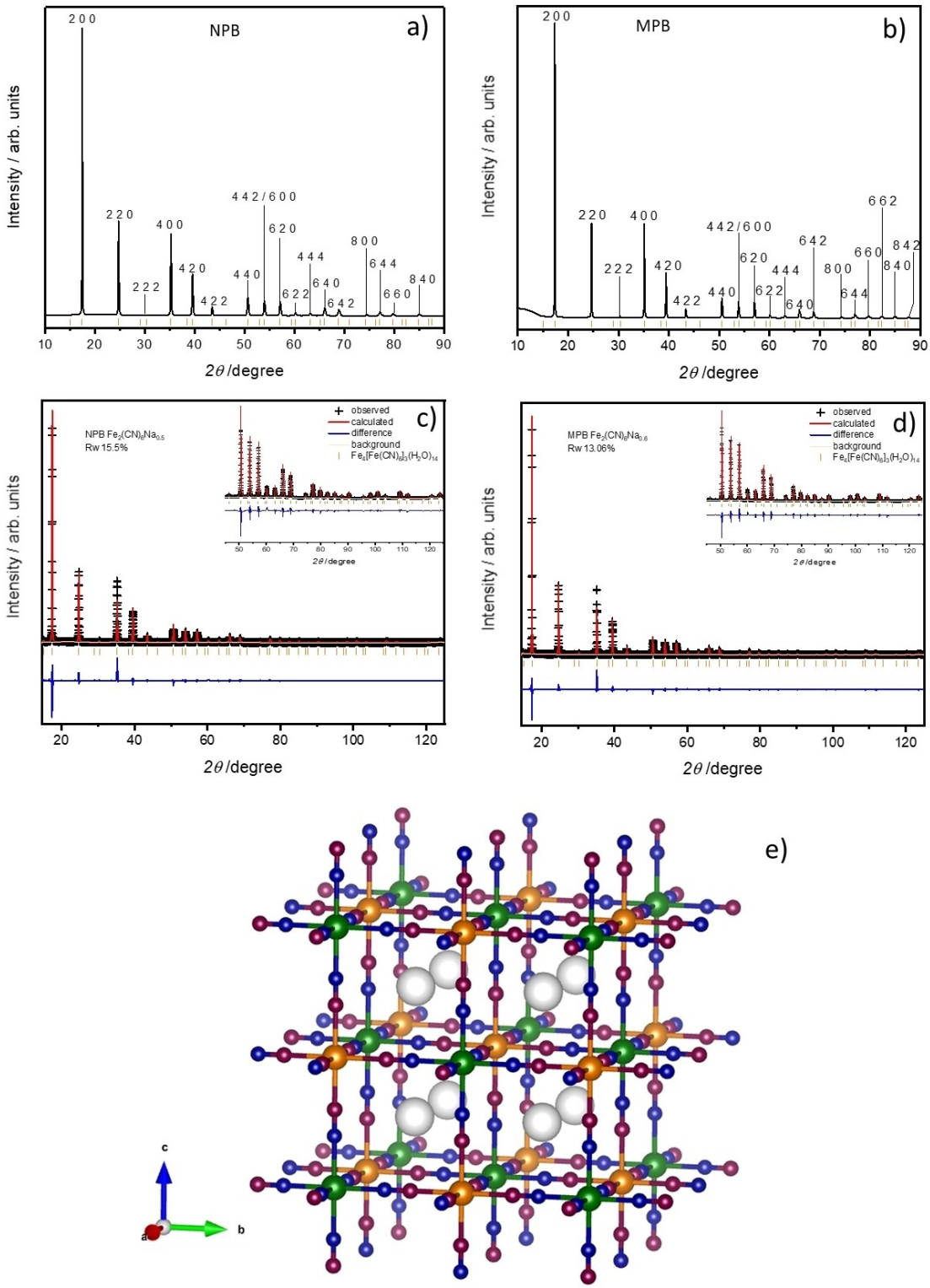

Figure 2. (a) Diffraction patterns of NPB and (b) MPB fitted with WinPlotr-2006 software and with Miller indexing of the planes. Rietveld refinement of (c) NPB and (d) MPB powder diffraction patterns. (e) Schematic structure of Prussian blue (Na in white, C in purple, N in blue, Fe1 and Fe2 in green and orange, respectively.

Moreover, in order to evaluate the electrochemical performances of the synthesized cathodes, coin cells were assembled in an Ar-filled glovebox using sodium metal as counter electrode and Whatman GF/ D soaked in $NaClO_4$ 1 M in EC/PC (1 : 1, v/v) as separator and electrolyte. The PB/ liquid electrolyte/ Na cell was tested in the 2.5 to 4.3 V potential range while applying a current density equivalent to C/10 (1 C = 170 mAh g^{-1}). Figures 3a, e show the galvanostatic charge/discharge profiles of

Table 3. Unit cell parameters, size, strain and Rietveld refinement data calculated for NPB and MPB.

Sample	NPB	MPB
Cu Kα radiation wavelength (Å)	1.54060	1.54060
Empirical formula	$Fe_2(CN)_6Na_{0.5}$	$Fe_2(CN)_6Na_{0.6}$
Formula weight (g mol^{-1})	280.8	282.2
Crystal system	Cubic	Cubic
Space group	Fm-3m (225)	Fm-3m (225)
a = b = c (Å)	10.1927 (2)	10.1996 (1)
α = β = γ (°)	90	90
Volume (Å^3)	1058.92 (2)	1061.08 (4)
Crystal density (g cm^{-3})	1.76	1.77
Z (cell formula units)	4	4
T (°C)	25	25
Pattern range, 2θ (°)	14.55–125	14.55–125
Weighted profile R-factor, Rwp (%)	15.49	13.06
No. of data	5362	5364
Size (nm)	550	909
Strain (%)	0.4	0.3

NPB and MPB respectively; where two plateaus at 3 V and 3.5 V are clearly visible and could be ascribed to the Fe^{2+}/Fe^{3+} redox couple; in particular, the two distinct plateau are generated by two iron atoms with different coordination, which are in a high or low spin state depending on the ligand.[33] Both materials showed a limited initial specific capacity due to a lack of sodium within the structure, which is consistent with the Prussian blue sodium deficiency, thus confirming the estimation made by EDX and XRD. However, both NPB and MPB have demonstrated overall high capacity retention, 91.4% and 91.6% respectively, and low capacity fade after 100 cycles with still a remarkable efficiency of 96.3% and 98% (see Figures 3b, f). The materials were then tested at different C-rates to assess their stability at higher current densities and determine their rate capability. Figures 3c, g display the voltage profile obtained varying the current from C/10 to 1 C, the plotted curve corresponds to the fifth cycle at each current rate. The specific charge and discharge capacity for each cycle in the C-rate capability study is shown in Figures 3d, h. For both samples, an initial capacity efficiency above 100% is observed, which may be related to the sodium deficient character of Prussian blue structures. At low current densities, MPB has shown a slightly higher discharge capacity, however some activation cycles are necessary to obtain satisfactory efficiency. In both cases, increasing the current density results in higher cell efficiency, while marginally decreasing the specific capacity. However, rapid oscillations of the specific capacity were observed in MPB when cycled at 1 C (Figure 3h), which could be attributed to formation of dendrites. This behaviour was fully reverted when setting the current back to C/10, resulting in a full recovery of the initial capacity, with a slight decrease of the coulombic efficiency which could also be compatible with a certain degree of electrolyte degradation.

The C-rate capability tests of NPB compared with the specific capacity at each cycle agree with undesired side reactions, particularly during the first cycle, showing specific capacity difference which may be related to the reaction between the cathode surface and the conventional electrolyte. In fact, previous studies have shown that nanometric electrodes, having a higher reactivity, are more susceptible to side reactions with liquid electrolytes.[34–37]

The electrochemical process and the determination of the Na^+ ion diffusion coefficient of both NPB and MPB cathodes were studied in sodium cell by means of CV. Initially, three voltametric cycles at the constant scan rate of 0.1 mV s^{-1} have been performed to better evaluate the reversibility of the electrochemical process and the related profiles are shown in Figure S7. The CV curves for both, NPB and MPB (Figure S7 a and Figure S7 b, respectively), indicate the presence of two redox peaks centred at about 3.1 and 3.6 V vs. Na^+/Na during oxidation, and three redox peaks centred at about 3.6, 3.4 and 2.8 V vs. Na^+/Na during reduction, ascribed to the high-spin $Fe^{2+}(N)/Fe^{3+}(N)$ redox couple coordinated to the N atoms of $(C{\equiv}N)^-$ at low potential and to the low spin $Fe^{2+}(C)/Fe^{3+}(C)$ redox couple bonded to the C atoms of $(C{\equiv}N)^-$ at high potential, respectively.[38] It is worth noting that the low-spin peak has split, probably due to structural defects which could modify the chemical environmental of the metal.[21] Furthermore, the presence of most defined separation of the peaks for MPB respect to NPB could be associated to a more pronounced Na^+ insertion through a stepwise process, indicating slightly dissimilar Na^+ diffusion phenomena, related to the different particles dimensions, as evidence in Figures 4a, b.[21] Overall, the modest polarization of the CV profiles, in particular for NPB, and the high reversibility of the subsequent cycles indicates the formation of a suitable solid electrolyte interphase at the electrode surface, as further clarified in Figure 5.[39] Moreover Figure 4 a, b reveals the CV response at increasing scan rates. The values related to the current peaks (I_p) grow by increasing the scan rate (ν), as stated by the linear trend of I_p *vs.* $\nu^{1/2}$, thus suggesting sodium diffusion as rate-determining step of the redox processes (see Figure S8) for the correlated plots. The obtained values for the indexed peaks related to high-spin (peaks A1 and C2) and low-spin (peaks A2 and C1) Fe^{2+}/Fe^{3+} redox couple have been used to calculate the Na^+ diffusion coefficients for NPB and MPB, respectively, D_{CV} (cm^2 s^{-1}), according to the Randles–Sevcik method:[40]

$$I_p = 0.4463zFAC\sqrt{\frac{zF\nu D_{CV}}{RT}} = 2.686 \cdot 10^5 AC\sqrt{z^3\nu D_{CV}}$$

where I_p is the peak current value (A), $z = 2$ is the number of exchanged electrons, F is the Faraday constant (96485 C mol^{-1}), A is the electrodes geometric area (0.636 cm^2), C is the Na^+ concentration within the cubic structure of PBs (mol cm^{-1}), ν is the scan rate (V s^{-1}), R is the gas constant (J K^{-1} mol), and T is the temperature (T = 298.15 K). The obtained values of D_{CV} for NPB and MPB are shown in Figures 4c and Figure 4d, respectively, and are calculated by considering the I_p *vs.* $\nu^{1/2}$ linear slope of the high-spin (Fe^{HS}) and low-spin (Fe^{LS}) Fe^{2+}/Fe^{3+}

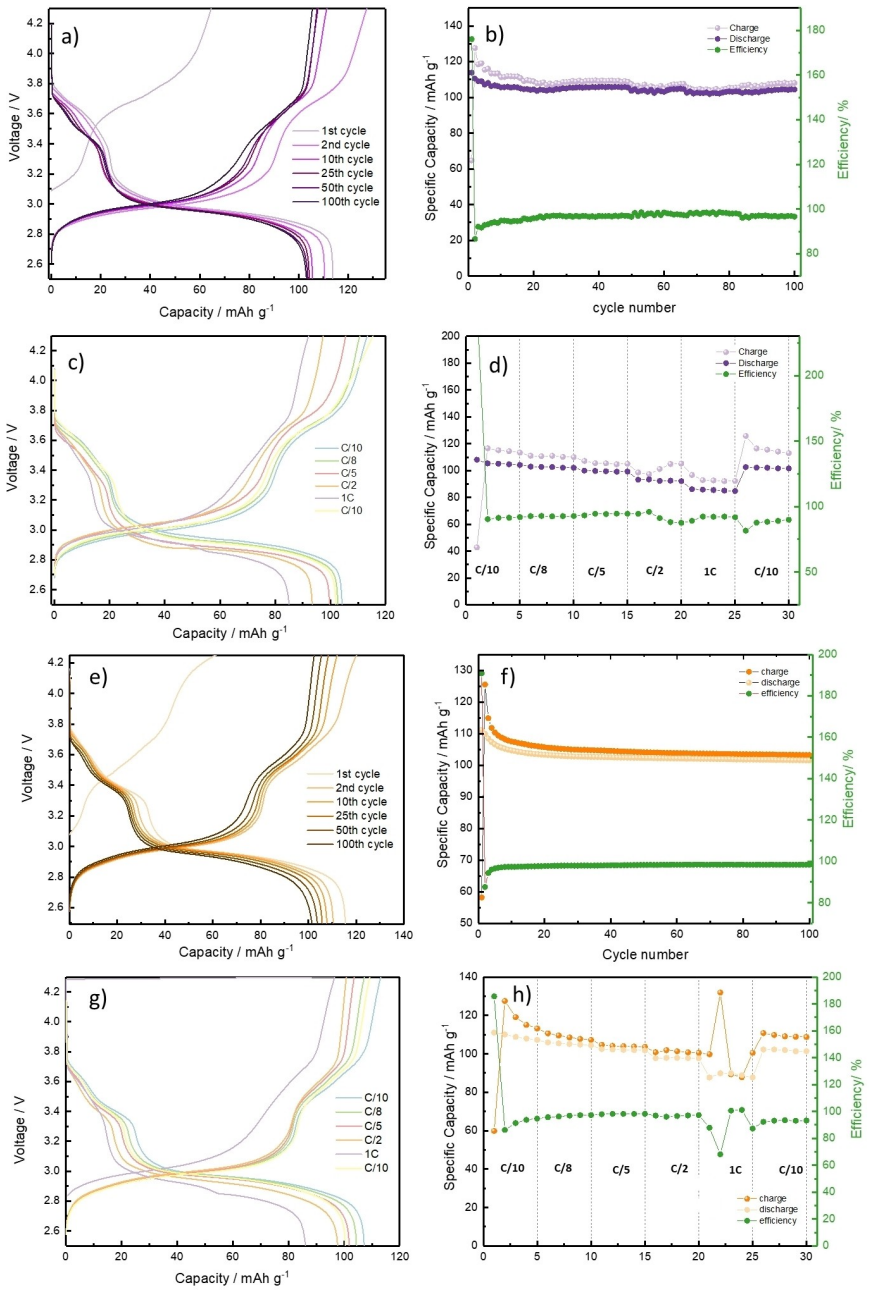

Figure 3. Electrochemical cycling performances evaluated within a voltage window of 2.5–4.3 V, while cycling the cell at a C-rate of C/10. (a, b) charge-discharge profile and cycling trend of NPB, (c, d) charge-discharge profile after 5 cycles at each current density and cycling trend at different current densities of NPB. (e, f) charge-discharge profile and trend of MPB at C/10, (g, h) charge-discharge profile after 5 cycles at each current density and cycling trend at different current densities of MPB.

current peaks during charge and discharge, as illustrated in Figure S8. The results of Figures 4c and Figures 4d indicate faster reaction kinetics for sodium storage for the Fe^{HS} compared to Fe^{LS} in both samples, result in good agreement with others found in literature.[41,42] Furthermore, NPB presents higher D_{CV} values (at about 10^{-11} $cm^2 s^{-1}$) compared to MPB (at about 10^{-12} $cm^2 s^{-1}$), indicating that the different particle dimensions (nanometric for NPB and micrometric for MPB) together with the different diffusion mechanism described before, affect the diffusion coefficients of the samples.[21]

In order to further investigate the effect of particle size on the interfacial properties upon cycling, impedance measurements were performed on both NPB and MPB electrodes during the 1st, 25th and 50th cycle at a bias potential of 3.4 V (i.e., between the two main processes of the PB cathode). The obtained Nyquist dispersions, shown in Figure 5a, b, consist of three main common features: I) a high-frequency intercept with the real axis; II) a medium-frequency semicircle; III) a low-frequency line related to solid-state diffusion. Based on the obtained data, the Nyquist plots have been modeled by the Equivalent Circuit Method (ECM) and fitted through a non-linear

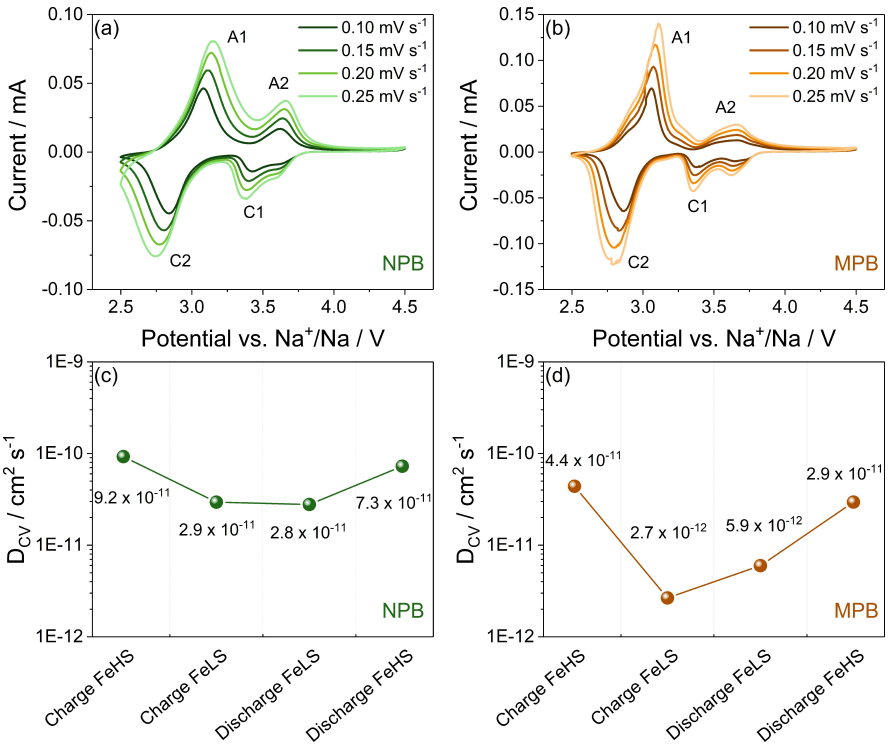

Figure 4. CV profiles with indexed peaks of (a) NPB and (b) MPB in Na cell at scan rates (ν) of, 0.1, 0.15, 0.2, and 0.25 mV s^{-1} Potential range 2.5–4.5 V vs. Na^+/Na. Trends of DCV (diffusion coefficients from CV) at various SoC for (c) NPB and (d) MPB.

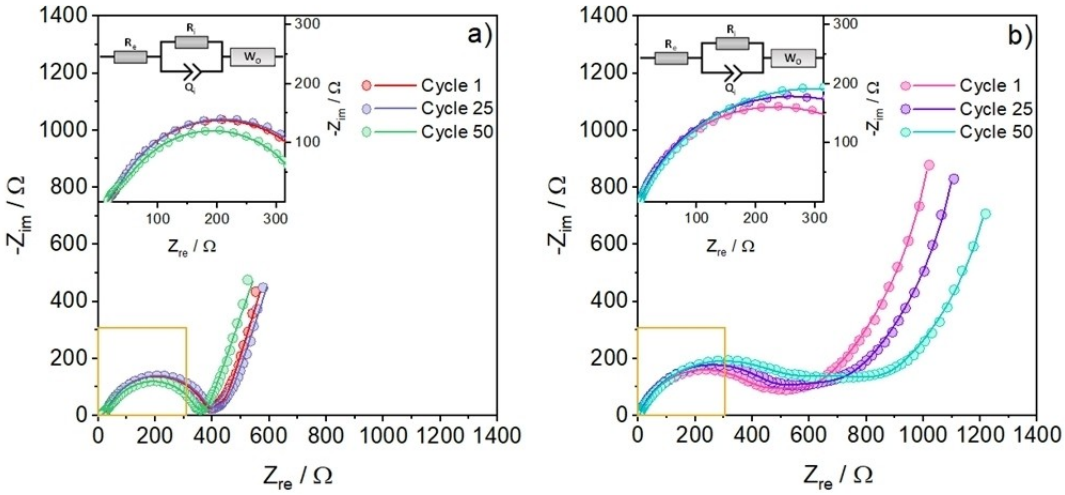

Figure 5. Nyquist plots and related fits obtained from EIS measurements at 3.4 V during the 1st, 25th and 50th galvanostatic cycles for (a) MPB and (b) NPB, both employing 1 M $NaClO_4$ in EC:PC liquid electrolyte. The insets show magnification in the high-frequency region. A representation of the equivalent circuits used for the fitting is displayed above each graph.

least-squares (NLLS) protocol.[43,44] The high-frequency intercept represents the Na^+ ion migration through the electrolyte medium, and it was modeled by a pure resistor element (R_e). The medium-frequency semicircle represents the overlapping interfacial resistances related to Na^+ ion migration through the electrolyte interphases and the faradaic charge-transfer processes, coupled with double layer capacities at both electrodes. The semicirle was modeled as a resistor element (R_i) in parallel with a capacitor element (C_i). Finally, the low-frequency line represents a finite solid-state diffusion with reflective boundary, and it was modeled by a finite-space open Warburg element (W_O). The resulting equivalent circuit for MPB and NPB, expressed with Boukamp's notation,[43,44] is $R_e(R_iC_i)W_O$. For the fitting procedure, the capacitor element C has been substituted by a constant phase element Q to account for the non-ideal behavior given by surface roughness and electrode inhomogeneity.[45]

From the Nyquist plots in Figures 5a, b and the related fitted values in Table S4, both MPB and NPB display a low and stable electrolyte resistance upon cycling, with R_e values remaining basically constant. By considering the evolution of the R_i, the two samples display a marginally different behaviour: on one hand, MPB seems to have a resistance increase in the first 25 cycles followed by a decrease at cycle 50, indicating a progressive stabilization of the interphases and of charge transfer; on the other hand, the resistance values in NPB show a sharper increase during the first 25 cycles followed by a less pronounced increase at cycle 50, indicating a slower stabilization of the interphases. This can be rationalized by considering the particle size of the NPB electrode material, as smaller particles generally favour the charge transfer kinetics, but they also favour side-reactions with the electrolyte, thus making the stabilization of the interphases slower upon cycling. Nevertheless, this does not seem to affect the cycling performances of the samples, as they have very similar specific capacity and capacity retention (Figure 3).

Although no substantial differences in electrochemical behaviour were found by varying the particle size, both NPB and MPB have demonstrated satisfactory performances. In particular, the use of nanometric particles did not show a clear improvement on the cycling stability or better rate capability as expected,[36,46] which may be due to unfavourable interactions between the cathode and the conventional liquid electrolyte, triggered by the large surface area and thus high reactivity of the cathode particles. To prevent potential parasitic reactions between the cathode and the liquid electrolyte that might compromise the performance of the NPB, a PEO/PVDF based gel polymer electrolyte was synthesized. The use of GPE is expected to improved cell safety by decreasing the flammability risk of the liquid electrolyte and thus allowing a better evaluation of the electrochemical performance of the nanometric PB compared to the micrometric one.

Gel Polymer Electrolyte

PVDF was selected as polymeric base for the GPE composition, later combined with PEO to improve properties such as conductivity and flexibility. The phase inversion method was applied to maximize the surface area of the polymeric matrix and to increase the number of ionic conductors that can be accommodated in it, thereby improving GPE conductivity. Since toxic organic solvents, such as DMF or DMSO,[47,48] are frequently utilized, we have developed new synthetic strategy in which DMF solvent was replaced by acetone, which is a green, inexpensive, non-toxic, and environmentally friendly alternative. Acetone is often used to dissolve PEO, however, if used in excess, it can also dissolve PVDF. The solution was heated at 80 °C to ensure a better miscibility of the two polymers. Then, glycerol was chosen as non-solvent and added dropwise to the polymeric slurry. As a highly volatile solvent, acetone evaporates rapidly, whereas glycerol evaporates more slowly, creating some holes in the structure and thus resulting in significant porosity that can be observed by SEM analysis. In particular, Figure 6a reveals a homogeneous distribution of pores throughout the membrane, and, at higher magnifications (Figures 6b, c), it can be seen that, even within the surface pores, there is a large interconnected network of cavities in which the liquid electrolyte can be stored. SEM mapping demonstrated that both PEO and PVDF were evenly distributed as confirmed from the carbon signal (Figure 6d), together with the oxygen signal (Figure 6e), which is specific to polyethylene oxide and the fluorine one (Figure 6f), which is exclusively present in polyvinylidene fluoride. The spatial distribution of these two elements provides a valuable indication of the polymer distribution within the membrane, confirming the uniformity of the matrix. The effective dispersion of the polymers ensures a high pore density, thus promoting electrolyte uptake. Specifically, PEO displays a greater affinity for glycerol than polyvinylidene fluoride, as hydrogen bonds may be formed between the hydrophilic segments and glycerol. Thus, this kind of interaction allows a proper distribution of the non-solvent throughout the matrix, resulting in a favorable pore dispersion. However, excessive polyethylene oxide content can result in the phase separation of the PVDF and non-solvent, yielding parts that are polymer-rich or polymer-poor, as reported in the literature.[49–51]

FTIR spectroscopy was performed to analyze the membrane's vibrational modes that allow us to gather information on the molecular interactions and chemical bonding in our polymers. Figure 6g displays the obtained spectra for the two pristine polymers (blue and red) and the blended one (green). In Table 4, the main vibrational modes of the three polymers are summarized. Blended PEO-PVDF pattern proves to be a reasonable trade-off between the two starting materials as it contains the characteristic peaks of both polymers. In many cases, the signal of the pristine polymers can be found at same wavelength in the blended spectrum, for example the scissoring of CH_2 falls at 1342 cm^{-1} in both PEO and blend, as does the stretching of CF_2 at 1180 cm^{-1}, which occurs at the same wavelength in both PVDF and PEO-PVDF. Interestingly, other peaks have been shifted, including the characteristic peak of the CH-stretching of PEO (2876 cm^{-1}), which has shifted to 2883 cm^{-1} in the final polymer. Additionally, some signals in the fingerprint zone are the result of a perfect combination of several components, such as the peak at 531 cm^{-1}, which is the result of the overlapping of the peak at 529 cm^{-1} of PEO and the one at 532 cm^{-1} of PVDF. The blend's success is confirmed by the presence of new peaks not found in the pristine material, such as the one at 1200 cm^{-1} and absence of others, such as the peak at 947 cm^{-1} present in polyethylene oxide but not in the blend, which could be caused to specific interactions between PEO carbon and PVDF fluorine.[52] Furthermore, a clear indication of the blend's effectiveness is demonstrated by the presence of a very broad and weak peak at around 3500 cm^{-1}, which can be attributed to the formation of a hydrogen bond between the oxygen or hydrogen of the PEO and the fluorine of the PVDF.[53,54]

Moreover, to observe the IR non-active vibrational modes, the sample was further examined by Raman spectroscopy (Figure S9). To prevent polymer fluorescence, an infrared laser

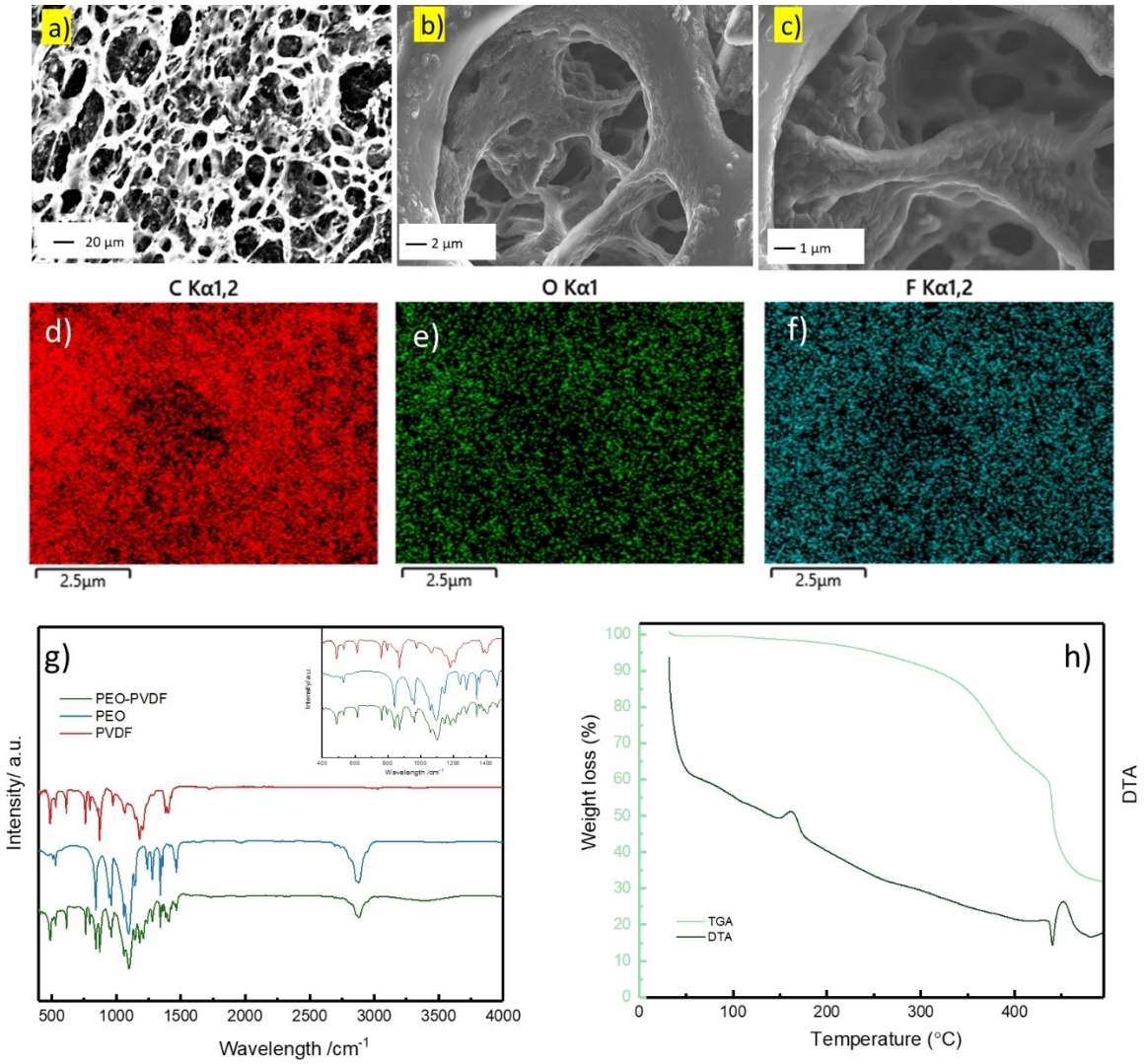

Figure 6. (a–d) SEM image of the blended PEO/PVDF membrane with higher magnification of the sample. Mapping of the spatial distribution of (d) carbon, (e) oxygen and (f) fluorine within the membrane. (g) FT-IR analysis in the 400–4000 cm^{-1} range and (h) TGA/DTA analysis performed under nitrogen flow in the 30 °–500 °C temperature range.

source was utilized. In agreement with previous observations, the spectrum obtained represents a satisfactory balance between the two original polymers; in particular, the bending of the CH_2 is still visible at 1485 cm^{-1}, the twisting of the CH bond can be located between 1260 cm^{-1} and 1240 cm^{-1}, the CO stretching is located at around 1085 cm^{-1}. Furthermore, a convolution of at least three contributions can be seen at 840 cm^{-1}: the stretching of the OH located in the terminal part of PEO chain, the rocking of CH_2 and the stretching of the CF_2 bond belonging to the PVDF portion.[52,55–58] The lack of additional peaks suggests a high purity of the polymeric matrix.

The thermal behavior of the membrane before impregnation in $NaClO_4$ 1 M in EC/PC (1 : 1, v/v) was investigated by means of TGA and DTA in the 30 °C–500 °C temperature range. The results are reported in Figure 6h. The TGA curve of the blended membrane exhibited an average thermal stability compared to the pristine polymers and a typical two-step decomposition profile was detected. An initial weight loss of approximately 3% can be found near 150 °C and it can be attributed to the loss of residual solvents or absorbed water, as suggested from the endothermic peak on DTA. The first step degradation starts at 345 °C, resulting in a loss of approximately 15% due to the starting decomposition of PEO. This is followed by a further weight loss of 40% at 430 °C because of PVDF decomposition. Anyway, it is worth noting that the blend demonstrated outstanding thermal properties; in fact, the polymers started to degrade at higher temperatures than when they are considered individually,[59,60] highlighting the presence of interactions between PEO and PVDF that stabilize the membrane. The thermal characteristics were further investigated by DSC analysis between 25 and 200 °C. Interestingly, an eutectic melting has been detected resulting in a single melting peak located at a different temperature than that of the pristine polymers.[61] The only exothermic peak is located at around 133 °C as shown in Figure S10, this value was given by the

Table 4. FTIR signals and vibration mode assignments of the PEO/PVDF blend.

Sample	Wavenumber (cm^{-1})	Mode assignment
PEO	2876	CH stretching
	1466	CH_2 scissoring
	1359	CH_2 fluctuating shake
	1342	CH_2 scissoring
	1279	CO twisting
	1241	CH_2 twisting
	1144	COC banding
	1096	COC banding
	1059	COC stretching
	961	CH stretching
	841	CO stretching
PVDF	3027	CH stretching
	2985	CH stretching
	1402	CF stretching
	1180	CF_2 stretching
	1067	CC stretching
	974	Phase α
	870	Amorphous phase
	795	CF_3 stretching
	760	Cristal phase
	612	Cristal phase
PEO-PVDF	3494	Hydrogen bond
	2882	CH stretching
	1467	CH_2 scissoring
	1406	CF stretching
	1360	CH_2 fluctuating shake
	1342	CH_2 scissoring
	1279	CH_2 twisting
	1181	CF_2 stretching
	1146	COC banding
	1099	COC banding
	1060	CO stretching
	962	CH stretching
	871	Amorphous phase
	841	CO stretching
	795	CF_3 stretching
	762	Cristal phase
	614	Cristal phase

combination of the melting temperatures of PEO (around 60 °C) and PVDF (around 177 °C).[62]

A crucial requirement for a gel electrolyte is the ability to store significant amounts of liquid electrolyte, ensuring high ionic conductivity. Thus, the electrolyte uptake of the membrane was assessed over a period of 3 hours as shown in Figure S11. The saturation is achieved within 30 minutes with an uptake rate of 227 %. The electrolyte absorption is influenced by several factors, including the interaction between the lithium salt or solvent used to formulate the electrolyte and the polymer matrix, which may affect the ability of the GPE to retain the electrolyte.[59,63,64] Furthermore, porosity is another crucial parameter because the greater the formation of holes, the better the electrolyte retention that will positively impact both, the ionic conductivity and electrochemical properties of the GPE.[50,51]

The electrochemical properties of the membrane were analysed by means of impedance spectroscopy as shown in Figure 7a. For this purpose, a symmetric cell configuration was used, and a Na/ electrolyte/ Na coin cell was assembled using both liquid electrolyte $NaClO_4$ 1 M in EC/PC (1 : 1, v/v) and the GPE soaked in $NaClO_4$ 1 M in EC/PC (1 : 1, v/v). The so obtained Nyquist plots were modelled by the Equivalent Circuit method through a non-linear-least-squares (NLLS) fitting protocol by using the RelaxIS3 software (rhd instruments).[65] The equivalent circuit $R_e(R_iC_i)Q_w$, written following Boukamp's notation,[43,44] was employed to take into account the different characteristic features of the spectra: Na^+ ions migration through the electrolyte (high-frequency intercept with real axis, R_e); contact resistance and Na metal interface resistance together with the related double-layer capacitances ($R_iC_i = R_1C_1 + R_2C_2$) and Warburg-type bulk solid-state diffusion (low-frequency line, Q_w). To account for the roughness and the inhomogeneities of the surface, the pure capacitive elements (C_1 and C_2) were substituted by constant phase elements (Q_1 and Q_2).[33] The main difference between the two spectra is the intrinsic resistance of the electrolyte, which is lower for the liquid ($7.6 \pm 0.2\ \Omega$) than for the GPE ($24.4 \pm 0.2\ \Omega$). This may depend on ion mobility since sodium ions can move more easily in the liquid medium than in the polymeric matrix allowing a faster motion and a lower resistance. Then, plating/stripping tests were conducted at 0.05 mA cm^{-2} (inset Figure 7a) to better understand the stability of the electrolytes. In both cases, the results showed a uniform and well-defined profiles for over 50 cycles with a low overpotential of approximately 8 mV for the GPE and 17 mV for the liquid electrolyte. In addition, no dendrites or irregular cycles were detected for any system, demonstrating good compatibility of the membrane with sodium metal.[66] However, in the gel electrolyte, a slight increase in overpotential can be observed as the cycles progress, this may be due to a thicker SEI (solid electrolyte interphase) formation compared to the liquid. Nevertheless, the resistance value is still remarkable and, despite the slight rise after 50 cycles, the overpotential is still lower than the liquid electrolyte, enabling the GPE to be used with a cathode for further applications.

The stability window of the electrolyte was investigated in the cathodic and in the anodic regions using a working electrode (WE) made of conductive carbon (P45) and PVDF (8 : 2) casted on aluminium and copper foils. The cell configuration used was WE/ electrolyte/ Na. For anodic stability, the potential at which membrane degradation begins was determined using linear sweep voltammetry (LSV). The remarkable stability of the electrolyte is shown in Figure 7b, remaining stable up to 4.70 V. This agrees with previous reports in the literature, which suggest that the degradation of the electrolyte, rather than that of the polymer matrix, is the limiting factor.[20]

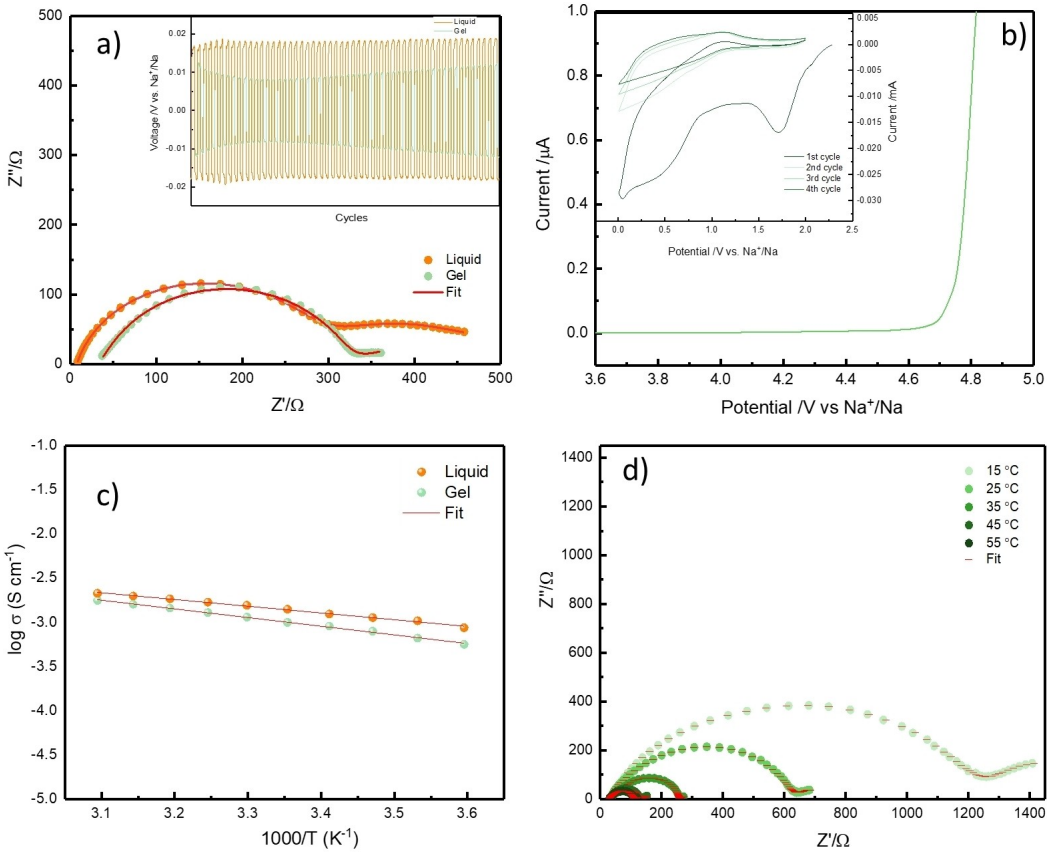

Figure 7. (a) PEIS and stripping and plating test (in the inset) of the liquid (orange) and gel (green) electrolytes. (b) LSV and CV (in the inset) obtained in WE/GPE/Na cell configuration. (c) Linear fitting of GPE (green) and liquid (orange) electrolyte Arrhenius plots. (d) GPE transference number calculation at 15 °, 25 °, 35 °, 45 ° and 55 °C.

Moreover, the stability window of the electrolyte was extended to the cathodic region by CV scans within 0.01–2 V voltage limits (insert Figure 7b). In particular, during the first cycle, an irreversible peak related to the formation of the SEI was detected. Indeed, the subsequent cycles showed an effective overlapping, indicating good process reversibility. It is worth noting that the identified peaks are exclusively attributable to the carbonaceous material of the working electrode. No additional signals related to the membrane are visible, confirming that no degradation has occurred. Thus, the GPE was estimated to be stable in the 0.01–4.70 V voltage range, enabling the membrane to become a suitable option for further electrochemical applications.

The ionic conductivity of the material was evaluated in the 5 °C to 50 °C temperature range. In order to better control the electrolyte's thickness, the membrane was placed into a Teflon ring and sandwiched between two stain-steel (SS) blocking electrodes in a SS/ electrolyte/ SS configuration. The Arrhenius plot in Figure 7**c** reveals that the conductivity values found for the GPE are very satisfactory even at room temperature, being only slightly lower than the conventional liquid electrolyte, and comparable at 50 °C. The ionic conductivity is influenced by several factors: firstly, porosity plays a fundamental role as a good presence of evenly distributed pores allows greater electrolyte uptake. Thus, as the movement of sodium ions is accelerated in the liquid phase compared to the gel phase, higher porosity improves electrolyte uptake, resulting in higher ionic conductivity.[51,67,68] Furthermore, the inclusion of polyethylene oxide in the blend composition may affect conductivity. This is because PEO is composed of repeating CH_2CH_2O units, which can easily coordinate sodium ions, thereby promoting the dissociation of sodium salts through the lone pair electrons of the oxygen atoms. Moreover, the beneficial effect of PEO has been previously suggested since the motion of sodium within PEO-based GPEs is achieved through interchain and intrachain hopping mechanism in which sodium ions can weakly bind the ether oxygen atoms in PEO and hop to closest coordinating sites through the segmental motions of the polymer chains.[2,69] On the other hand, polyvinylidene fluoride has both a high dielectric constant and electron-withdrawing groups that enhance the compatibility with polar organic solvent used for the conventional electrolyte formulations, this could promote the dissociation of the sodium salt and results in higher ionic conductivity.[70] Even the choice of the solvents trapped together with the sodium salt within the polymer matrix has an important effect on conductivity, actually the use of plasticizer with a high dielectric constant helps to minimize the Coulombic interactions between ions, preventing the formation of crystalline regions and ion aggregates and ultimately enhancing ionic conductivity.[71,72] Additionally, the

presence of carbonates reduces the structural order, and thus the crystallinity, of the polyethylene oxide amplifying the segmental movements of the polymeric chains. This effect is particularly evident as the temperature rises, the increased kinetic energy that the polymer acquires allows a greater bond rotation promoting greater inter-chain and intra-chain Na^+ ion hopping.[69,73]

It should be noted that, at low temperatures, the Arrhenius profiles of the conventional electrolyte and the GPE are quite close. A possible explanation of this phenomenon may be related to the introduction of a significant amount of plasticiser that affects the sodium transport mechanism, which is not predominantly related to polymer chain segmentation, but is dominated by liquid phase transport. As a result of the intricate ion conducting mechanism in GPEs, conductivity at varying temperatures cannot be solely explained by the Arrhenius law. In fact, two distinct contributions are often identified, which could be defined by both the Arrhenius law and Volger-Tammanan-Fulcher behaviour (VTF).[74] Moreover, the VTF model considers the conductivity associated with the relaxation and long-range motion of polymer chains. This is especially crucial at temperatures exceeding the polymers' melting point.[75,76] Furthermore, from the linear fitting of the conductivity plot, the slope was derived and then used to obtain the activation energy as following:

$$E_a = -R \times Slope$$

Where E_a is the activation energy, R is the gas constant, and the slope was obtained by the linear fit of the Arrhenius plot. Notably, the value obtained for the GPE is 8.15 ± 0.02 kJ mol^{-1}, which is quite similar to that of the conventional electrolyte (6.31 ± 0.02 kJ mol^{-1}).

The sodium ion transference number (t^+) in GPE was calculated by Bruce Vincent method (Figure 7d) and the value are reported in Table 5.

Although GPE's sodium ion transference numbers are typically not very high (approximately 0.2–0.4), they remain an important parameter for evaluating the gel polymer electrolyte's efficiency.[2] Notably, the values presented in Table 5 are satisfactory and consistent with those reported in previous studies.[77–79]

It is worth noting that conventional electrolytes present significant safety concerns due to the flammability risks associated with organic solvents. Since a significant quantity of liquid electrolyte is confined within the polymeric pores of the GPE, incorporating flame-retardant additives could represent an interesting strategy to enhance the overall safety of the system.[2] Usually, organic phosphorus compounds are considered one of the best choices.[80,81] Therefore, triethyl phosphate (TEP) was selected as a flame retardant and incorporated into the gel polymer electrolyte formulation.[82,83]

Table 5. GPE transference number at different temperatures calculated by Bruce Vincent method.

Temperature (°C)	I_0 (mA)	I_{ss} (mA)	R_0 (Ω)	R_{ss} (Ω)	t^+
15	0.017	0.008	1191.07	1162.76	0.21
25	0.035	0.278	656.01	583.74	0.35
35	0.099	0.062	219.9	284.66	0.37
45	0.136	0.085	146.85	164.43	0.39
55	0.205	0.137	98.58	81.44	0.41

Prussian Blue GPE Cell Configuration

Particles size plays a crucial role highly affecting the properties of the cathode materials, it is well known that increasing the surface area of the particles may have a positive effect on electrochemical performances.[46,84] Smaller particles can enhance ion diffusion by shortening the ion path through the electrode,[36] due to a decreasing of the time constant t in accordance with the relationship $t = L2/D$, where L is the diffusion length and D is the chemical diffusion constant in the solid state[85]; this effect also results in a lower concentration gradient and therefore less mechanical stress that could damage the material.[86] The electron path could also be reduced by reducing the size of the cathode particles, giving the cell greater cycling stability.[87] Moreover, it has been reported that improving the reaction area between the cathode and the electrolyte can increase the rate capability and the stability of the cell.[88–90] Unfortunately, a large surface area also results in higher reactivity of the nanometric particles that could cause multiple side reactions between the cathode and the electrolyte, this unwanted interaction could finally affect the performance of the cell. To limit undesired reactions and to accurately assess the real performance of the cathodic materials, the liquid electrolyte has been trapped within a polymeric matrix. This approach aims to prevent the possible dissolution of the cathode particles in organic solvents and to reduce side reactions which mostly occur for NPB. Furthermore, for the sake of clarity, a comparison was made with MPB under identical conditions, although it was expected that NPB would be more affected by the electrolyte change. The electrochemical performances of both cathodes were analysed in a quasi-solid-state cell configuration, using PEO/PVDF GPE as electrolyte and sodium metal as counter electrode. The galvanostatic cycling tests performed in the 2.5–4.3 V voltage window are reported in Figure 8a, b and 8e, f where the voltage profiles and the cycling trends are shown. As previously anticipated, MPB's electrochemical properties do not seem to be significantly affected by the change in the electrolyte, but rather the performances are consistent with the trend previously analysed for the conventional liquid electrolyte, or even slightly improved. The cell exhibited a remarkable stability in gel configuration, with a capacity fade of only 12.2% after 100 cycles and a high efficiency of 98.4%, a slight increase in comparison with the liquid electrolyte cell configuration (Figure 3e, f). Even when the current density is varied, the material did not exhibit any performance degradation ascribed to GPE. Like in previous tests, the cells required of some activation cycles at low C-rate before reaching the optimum coulombic efficiency (Figure 8g,

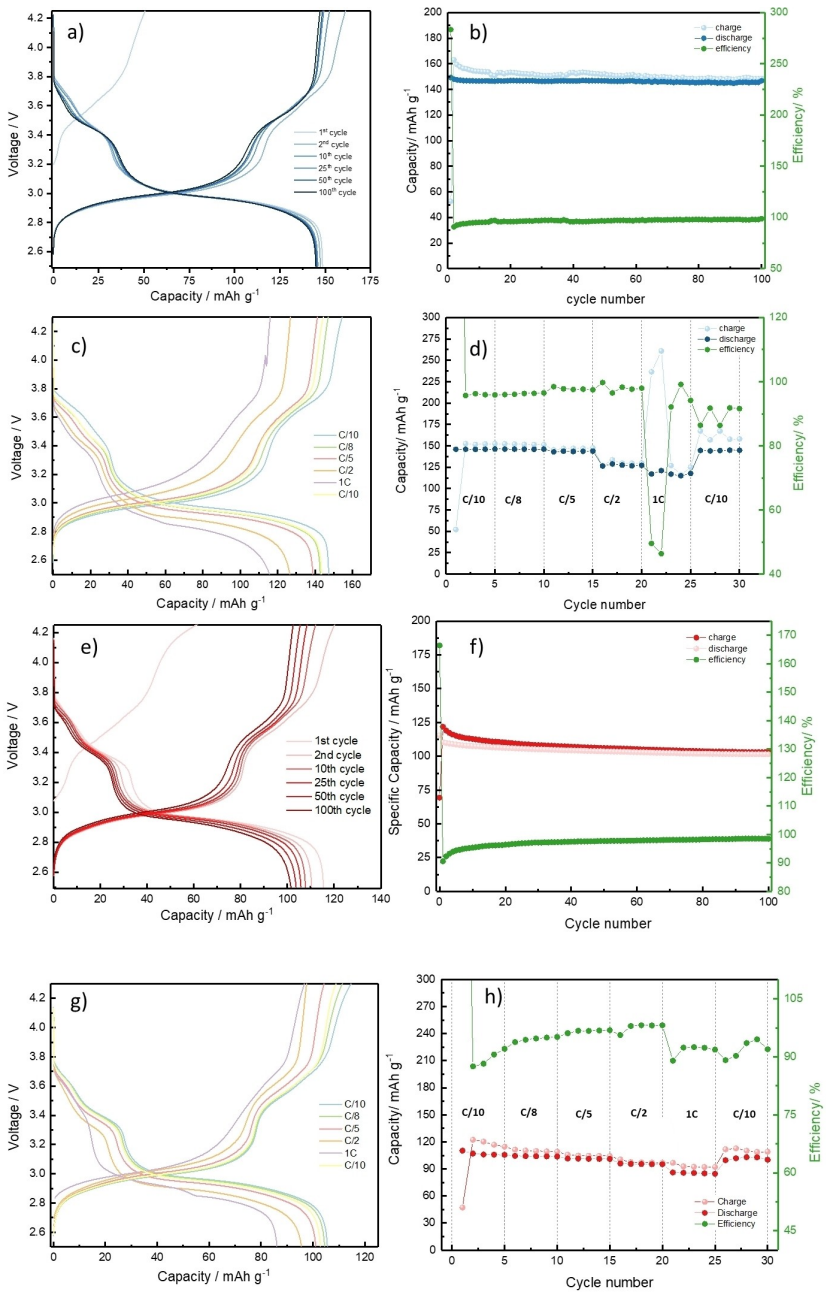

Figure 8. (a, b) Electrochemical cycling performances of PB cathodes in 2.5–4.3 V window, charge-discharge profile and trend of NPB/GPE/Na cell configuration at C/10. (c, d) Charge-discharge profile after 5 cycles at each current density and cycling trend at different current densities of NPB/GPE/Na. (e, f) Charge-discharge profile and trend of MPB/GPE/Na at C/10. (g, h) Charge-discharge profile after 5 cycles at each current density and cycling trend at different current densities of MPB/GPE/Na.

h). On the other hand, when small reactive particles, such as those of NPB, are exposed to the gel electrolyte, significant changes can be observed. Indeed, compared to liquid electrolyte cell configuration, the charge/discharge cycling performances are enhanced. In particular, Figure 8a, b displays the galvanostatic cycling tests performed in the NPB/GPE/Na configuration where a capacity of nearly 150 mAh g^{-1} is reached and maintained for 100 cycles with a capacity fade of only 1.7% and an efficiency of 98.77% after 100 cycles. This demonstrates an effective sodium-ion insertion/extraction process suggesting possible synergistic effects between NPB and the gel polymer electrolyte, in contrast to the standard liquid electrolyte. Moreover, Figure 8c, d shows that increasing the current densities from C/10 to C/5 does not significantly affect the specific capacity of the material, which remained stable at around 145–150 mAh g^{-1}. However, an increase in the C-rate up to 1 C placed a significant stress on both the cathodic material and the polymer membrane, resulting in the formation of some dendrites which affect the cycling of the cell.

The performance of the NPB/GPE/Na cell was further assessed over an extended cycle life at C/2 (see Fig. S12). After 240 cycles, the observed capacity loss was about 14.8% with an

efficiency near to 100 %, confirming the promising properties of NPB/GPE/Na cell configuration even at higher current densities.

Furthermore, to enable a direct comparison between NPB-gel and previously reported Prussian Blue materials, Table 6 displays the electrochemical performance of other PB cathodes found in the literature.

Not only NPB/GPE/Na cell configuration displayed superior performances outperforming both NPB and MPB in liquid electrolyte cell configuration, but it also appears particularly attractive from a safety point of view, since the confinement of the electrolyte within the pores of the polymeric matrix reduces the flammability and thus the risk of ignition of the electrolyte. The use of GPE has led to an outstanding improvement of the electrochemical performance the nanometric cathodic material, however, the reasons for this improvement are currently under investigation, and the exact mechanism is not yet fully understood. Furthermore, the formation of an interesting cathode-electrolyte interphase (CEI), which could modify the reactivity and stabilize the cathode surface, may play a crucial role.[93] The CEI is primarily formed through the degradation of the electrolyte, resulting in a thin layer over the positive electrode made up of several decomposition compounds; this deposition process could take place both, during the initial cycles or directly through the GPE/NPB contact.[94] Establishing a stable CEI could have multiple positive effects such as the reduction of the interfacial resistance and of the metal dissolution, the prevention of electrode damage and the suppression of side reactions between the cathode surface and the electrolyte,[93,95,96] ultimately resulting in improved electrochemical performance and enhanced cell stability. Therefore, although the study of the CEI can be extremely challenging due to its complex composition and its dependence on electrolyte's nature, it is reasonable to assume that the introduction of a polymer electrolyte may alter the CEI with the introduction of new decomposition products in comparison to the bare liquid electrolyte. Previous studies have reported that polyvinylidene fluoride, commonly used as electrode binder, can spontaneously interact with metallic sodium via oxidation-reduction reaction, resulting in the formation of a particularly NaF-rich CEI.[97,98] This method has been successfully employed to prepare Prussian blue cathodes coated with an artificial NaF-rich CEI.[97] NaF plays a key role in CEI composition because it not only prevents parasitic reaction onto the Prussian blue surface, but it also induces a fast charge transfer.[94,99,100] Thus, it is reasonable to assume that this effect can be further enhanced by introducing PVDF as a copolymer into the polymeric matrix of the electrolyte.

In order to characterize the interfacial behaviour of the electrolyte medium when combined with nanometric particles in the cathode, impedance measurements were performed on NPB vs Na cells during the 1st, 25th and 50th voltammetric cycle at the discharged state (i.e., 2.5 V), employing either a 1 M $NaClO_4$ in EC:PC liquid electrolyte or a PEO/PVDF-based gel electrolyte, as shown in Figure 9a, b. For the cell containing the liquid electrolyte, a behaviour similar to that reported in Figure 5b was oserved, with a single semicirle including all capacitive and faradic phenomena. In contrast, for the NPB/GPE/ Na cell, two distinct medium-frequency semicircles could be observed: the first small semicircle at higher frequencies represents the interfacial resistance due to electrolyte interphases at the electrodes and/or particle-particle and particle-current collector contact resistance with associated charge accumulations, whilst the second semicircle at lower frequencies is associated with faradaic charge-transfer process coupled with electrical double layer formation. Hence, the two semicircles were fitted with two parallels $(R_1C_1)(R_2C_2)$, to account separately for both contributions. Also in this case, the capacitor elements have been substituted by constant phase elements (Q) during the fitting procedure, to account for the non-ideal behavior given by surface roughness and electrode inhomogeneity.[45]

From the Nyquist dispersions in Figure 9 a, b and the related fitted values in Table S5, both samples display a relatively stable R_e polarization upon cycling, with higher absolute values for NPB-Gel as compared to MPB-Liq due to the higher viscosity of the gel electrolyte. By considering the R_e evolution, the values of LB-Liq stay almost constant, with a slight increase of 7.9 % when going from cycle 1 ($R_e = 11.4\ \Omega$) to

Table 6. Electrochemical performances of previously reported Prussian Blue cathodes.

Samples	Potential [vs Na^+/Na]	Capacity	Cycling stability	Ref
$Na_{1.73}Fe[Fe(CN)_6]_{0.98}\ H_2O$	2–4 V	105 mAh g^{-1} at 100 mA g^{-1}	64 % after 400 cycles	[18]
$Na_{1.12}Fe[Fe(CN)_6]_{0.92}\ H_2O$	2–4 V	97 mAh g^{-1} at 100 mA g^{-1}	41 % after 400 cycles	[18]
$Na_{1.59}Fe[Fe(CN)_6]_{0.9}\ H_2O$	2–4 V	128 mAh g^{-1} at 10 mA g^{-1}	73.4 % after 200 cycles	[38]
$Na_{1.76}Fe[Fe(CN)_6]$	2–3.8 V	80–85 mAh g^{-1} at 100 mA g^{-1}	98.9 % after 200 cycles	[91]
$Na_{1.76}Fe[Fe(CN)_6]$ 2.6 H_2O	2–3.8 V	80–85 mAh g^{-1} at 100 mA g^{-1}	83.7 % after 200 cycles	[91]
$Na_{0.517}Fe[Fe(CN)_6]_{0.85}$ 3.15 H_2O	2–4 V	90 mAh g^{-1} at 50 mA g^{-1}	N.A.	[92]
$Na_{0.647}Fe[Fe(CN)_6]_{0.93}$ 2.6 H_2O	2–4 V	90 mAh g^{-1} at 2000 mA g^{-1}	90 % after 2000 cycles	[92]
$Na_{1.53}Fe[Fe(CN)_6]$ 4.2 H_2O	2–4 V	95–100 mAh g^{-1} at 100 mA g^{-1}	66 % after 200 cycles	[24]
Na1.73Fe[Fe(CN)6] 3.8 H_2O	2–4 V	100–105 mAh g^{-1} at 100 mA g^{-}	71 % after 500 cycles	[24]
$Na_{1.95}Fe[Fe(CN)_6]_{0.93}\ H_2O$	2–4 V	120 mAh g^{-1} at 50 mA g^{-1}	81.1 % after 150 cycles	[37]
$Na_{1.63}Fe[Fe(CN)_6]_{0.87}$ H_2O	2–4 V	120 mAh g^{-1} at 50 mA g^{-1}	66 % after 150 cycles	[37]

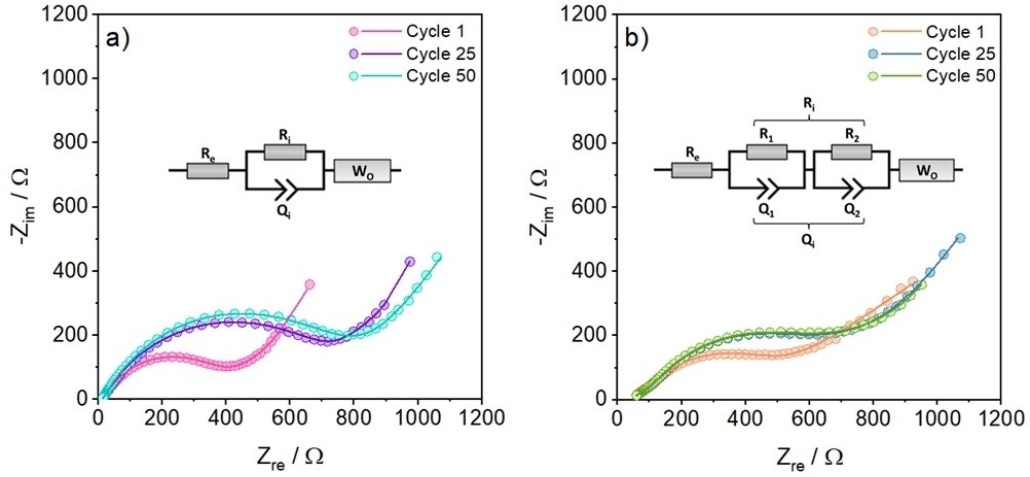

Figure 9. Nyquist plots and related fits obtained from EIS measurements at 2.5 V during the 1st, 25th and 50th voltametric cycles for NPB employing (a) 1 M $NaClO_4$ in EC:PC liquid electrolyte and (b) PEO/PVDF gel electrolyte. A representation of the equivalent circuit used for the fitting is displayed for each tested cell.

cycle 50 ($R_e = 12.3\ \Omega$); on the other hand, the associated R_e values for NPB-Gel display a decrease of 4.2% during the same cycling progression, from 43.4 Ω at cycle 1 to 41.6 Ω at cycle 50, thus indicating a faster and more pronounced stabilization of the electrolytic medium upon cycling. As for the polarizations associated to the semicircles, it is worth noting that the related absolute resistance values in the two samples cannot be directly compared, especially in two-electrode configuration, due to their dependence on the thickness and roughness of the Na metal counter-electrode, here not controlled, and the absence of a reference electrode. This renders impossible the separation of the SEI/CEI and charge transfer contributions from working and counter-electrode.[101–103] Moreover, the R_1 and R_2 features only display a slight separation of the contributions in the NPB/gel system, while, for all the cells with liquid electrolyte, they are completely overlapped. Nevertheless, the variation of the total R_i upon cycling, expressed as percentage increase/decrease relative to their initial values, can be more easily compared. Indeed, when considering the overall resistances coming from the semicircles (i.e., R_i), LB-Liq displays an initially pronounced increase up to 25 cycles with a less sharp increase at cycle 50, indicating a progressive stabilization of the interphases, possibly with electrolyte interphases dissolving and reforming, but an overall increase of 44.9% as compared to the initial value. In stark contrast, LB-Gel displays a much slower variation, with an overall increase of only 10.6% at cycle 50 with respect to cycle 1. These results suggest a better stabilization of the interphases when the gel electrolyte is employed together with smaller cathode particles, in agreement with the improved cycling performance displayed by the NPB-Gel system. This behavior can be tentatively explained by considering possible reactions between the employed cathode and gel electrolyte, as interactions between the –CN– group from Prussian blue analogues and F atoms from PVDF have already been observed.[104] Moreover, recent studies employing a PVDF-based membrane also showed that direct contact between Na metal and PVDF is likely to induce the formation of NaF, which is reported to stabilize the SEI and suppress dendrite formation at the counter-electrode side.[105,106] Based on these observations, it is reasonable to assume that the PVDF blended within the electrolyte membrane either provides stabilization of the SEI at the Na metal side or stronger interactions with the cathode active material, with formation of more inorganic and ionically conductive NaF-based electrode-electrolyte interphases at both sides. Nevertheless, the obtained results suggest a high compatibility of the PB cathode with the employed PEO/PVDF gel electrolyte, also for applications in Na-metal cells.

In order to confirm the presence of a sodium fluoride-rich CEI layer onto NPB electrodes when tested together with the GPE, X-Ray photoelectron spectroscopy measurements were carried out. Five samples were analysed to determine the fluorine content: pristine electrode, electrode in contact with the liquid electrolyte at open circuit voltage (OCV-liquid), electrode cycled with liquid electrolyte (cycled-liquid), electrode in contact with the gel polymer electrolyte at open circuit voltage (OCV-GPE) and the cycled electrode with the GPE as electrolyte (cycled-GPE). In particular, the high-resolution F 1s peaks are reported in Figure 10. Since PVDF is used as binder during electrode preparation, all the samples exhibited a typical C–F signal around 687 eV. For both, pristine and OCV-liquid electrodes (Figure 10a–b), almost the 95% of the fluorine contained in the sample was bound to carbon, indicating that the binder-related C–F peak predominates. However, when the same electrode is cycled (Figure 10c), a CEI layer may be formed as suggested by the intensity increase of the NaF peak, with half of the detected fluorine bonded to sodium, which is ascribed to a moderate presence of NaF. Interestingly, when the GPE is used (Figure 10d–e), large amounts of NaF are detected, with more than 80% of the total fluorine bonded to Na. The CEI rich in sodium fluoride is visible in both OCV and cycled samples, indicating that the passivation layer was spontaneously formed by reaction between Na and/or Na-containing species with fluorinated binder under polarized environment, inducing the formation of NaF. XPS analysis confirms that a CEI

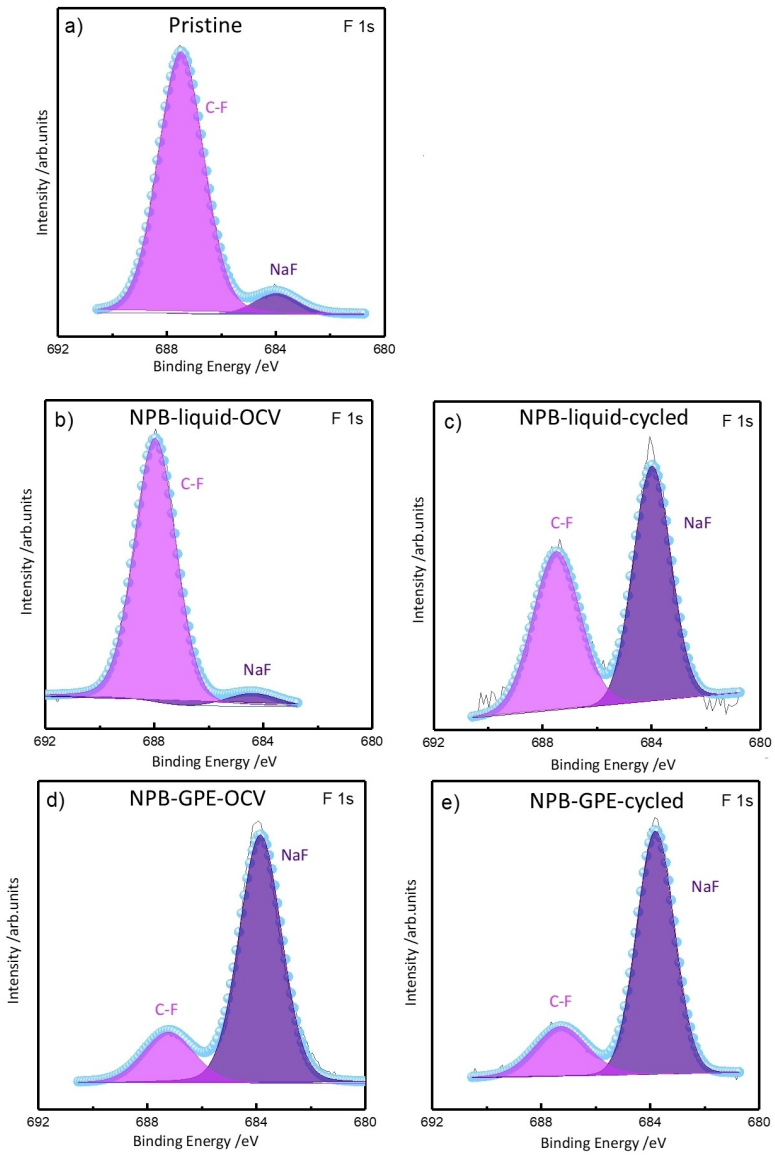

Figure 10. XPS F 1s peaks, experimental data (circles) and fitting deconvolution of (a) pristine electrode, (b) electrode in contact with the liquid electrolyte at the open circuit voltage, (c) electrode cycled with liquid electrolyte, (d) electrode in contact with the gel polymer electrolyte at the open circuit voltage and (e) cycled electrode with the GPE as electrolyte.

is formed in the NPB/GPE/Na cell and this type of passivation layer allows a better stabilization of the cathode surface while decreasing NPB-electrolyte unwanted side reactions, thus explaining the previously obtained improved cycling stability and specific capacity as shown in Figure 8a–b.

Conclusions

In conclusion, a nanometric and a micrometric cathodes were successfully synthesized, fully characterized and tested in a PB/ $NaClO_4$ 1 M in EC:PC (1 : 1 v/v)/ Na cell configuration. Even if the electrochemical performances were quite satisfactory, side reaction between NPB and the conventional electrolyte were detected, and, furthermore, the use of liquid electrolyte rises safety concerns. For this reason, a gel polymer electrolyte (GPE) made from PEO/PVDF using an eco-friendlier phase inversion technique with non-toxic solvents was prepared. The stability of the GPE was assessed in a symmetric cell before further investigation by means of CV, LSV, CA, PEIS, TGA, DSC, Raman and FT-IR spectroscopy. Both NPB and MPB have been tested in a quasi-solid-state configuration with enhanced safety characteristics, where the liquid electrolyte has been replaced by GPE, and the results of the cycling and rate capability tests have shown excellent performance for the NPB/ GPE/ Na cell configuration with a remarkable capacity retention, high Coulombic efficiency and improved specific capacity. Moreover, almost no capacity loss was detected for at least 100 charge-discharge cycles, outperforming the liquid electrolyte cells configuration as confirmed by PEIS measurements where a more stable interfacial behaviour seems to be promoted. This notable stability could be due to the formation of a NaF-rich CEI

as confirmed by XPS analysis that could modify the reactivity and stabilise the cathode surface thanks to the spontaneous reaction between sodium and PVDF. In particular, NPB/ GPE/ Na cell has demonstrated efficient sodium-ion insertion/extraction processes thus suggesting a remarkable synergy between the nanometric cathode particles and the synthesized gel polymer electrolyte, in contrast to the standard liquid electrolyte. Although further in-depth studies are still needed, we believe that the data obtained in the present work could be a starting point towards a more complete understanding and optimization of the nanosized Prussian Blue-Gel system for possible applications in Na-metal cells.

Despite both cells exhibiting decreased specific capacity at higher currents, this phenomenon appears to be highly reversible, confirming the presence of a robust scaffold useful for sodium insertion, and encouraging further application of PB in sodium-ion batteries.

Experimental

NPB was synthesized as follow: 2 mmol of $Na_4Fe(CN)_6x10H_2O$ were dissolved in 100 mL deionized water, then a solution of HCl (0.15 M) was prepared and added dropwise in order to promote the reaction. The mixture was maintained under vigorous stirring and heated at 60 °C for 5 hours until a dark blue solution was obtained (see Figure S13). The suspended powder was collected by filtration and washed several times with distilled water and ethanol before to be dried at 120 °C for 36 hours under vacuum in a Buchi oven.

MPB was produced using a similar procedure to that described above, however, the stirring time was increased to 24 hours in order to modulate the particle size.

The slurry was obtained by grinding the Prussian blue with a mortar and mixing it with conductive carbon (Super C65) and PVDF (7:2:1 respectively) using NMP as solvent. The mixture was stirred for 5 hours until an homogeneous slurry was obtained. The slurry was then casted onto an aluminum foil, dried at 70 °C in order to remove the solvent, cut in 9 mm disk electrode and dried again at 120 °C under vacuum for 3 hours in a Buchi oven. The electrodes were then transferred and stored into an Ar-filled glovebox (O_2 and H_2O level < 0.8 ppm).

The GPE was synthesized by phase inversion technique. 200 mg of PEO were first dissolved in 100 mL of acetone under vigorous stirring, then 200 mg of PVDF were added and the temperature of the reaction was raised to 85 °C. When all the PVDF was dissolved, 5 mL of glycerol were added, and the mixture was kept under magnetic stirring for 4 hours under reflux. 5 mL of triethyl phosphate (TEP) were used as a flame-retardant to improve membrane safety and reduce the flammability of the liquid electrolyte. The prepared slurry was cast onto a Teflon disk to enable acetone and glycerol to evaporate in turn and achieve the desired porosity. The membrane was kept in the oven overnight at 60 °C to ensure complete solvent evaporation. Thereafter, it underwent vacuum treatment for 5 days to remove all non-solvent residuals. The obtained self-standing membrane was cut in 9 mm disk and dried again into a Buchi oven at 50 °C for 15 hours before transferring it into an Argon filled glove box.

X-ray powder diffraction (XRPD) patterns were collected with the Cu–Kα radiation on a Bruker D8 Advance diffractometer in Bragg-Brentano geometry, equipped with a Lynxeye XE–T detector. The long fine focus (LFF) tube was operated at 40 kV and 40 mA. Data were collected in the 4–125° 2θ range using a 0.02° 2θ step scan and 5 s counting time. The powder samples were side loaded in a sample holder. Qualitative phase analysis was performed by applying a search and match procedure with the help of the PANalytical X'Pert Highscore program and the Crystallography Open Database (COD). The unit cell was calculated by Treor90 and Dicvol06 programs in FullProf Suite[107] after a fitting of the diffraction patterns using WinPlotr-2006 software[108]* and the space group was obtained by the help of Checkcell. The structure was solved ab initio with the direct methods implemented in Expo 2014 software.[109] Rietveld refinement of the structure model was performed using GSAS-II software.[110]

The morphology of the cathodes and of the electrolyte have been investigated through Scanning Electron Microscope (Zeiss Sigma 300 FM-SEM).

Fourier-transform infrared spectroscopy (PerkinElmer Frontier- FTIR) and Raman spectroscopy (Horiba HR 320) equipped with a IR laser (1064 nm) source was used to better investigate the vibrational mode of the functional group of the polymeric matrix. Instead, Raman experiments on PB samples were performed using a green light laser (532 nm) as source.

Thermal gravimetric analysis (TGA) was performed in the 30 °–500 °C temperature range under nitrogen flow and with a heating rate of 10 °C min^{-1} (PerkinElmer STA6000 TGA-DTA). In addition, the thermal properties of the membrane were studied by means of differential scanning calorimetry (DSC TA 250) analysis between 30 °C and 200 °C using a heating and cooling ramp of 10 °C min^{-1}.

CHN analysis was carried out in order to determinate the elemental composition of the two cathodes using a Fisons Instruments EA-1108 CHNS–O elemental analyser (Thermo Fisher Scientific Inc.)

ICP measurements were conducted utilizing a Thermo Scientific iCAP PRO ICP-OES (inductively coupled plasma-optical emission spectrometry) instrument.

The electrolyte uptake was determined as follow: the dry membrane was first weighted and then soaked in the liquid electrolyte ($NaClO_4$ 1 M in EC/PC (1:1, v/v)). After a while, the polymer was collected, dried with paper towels and weighed again. This process was repeated at various time intervals to determine the maximum amount of electrolyte that could be stored in the polymer.

All electrochemical tests were performed using 9 mm disk electrodes in CR2032 coin cells assembled in an Ar-filled glovebox (Jacomex GP Campus with O_2 and H_2O level < 0.8 ppm). Potentio electrochemical impedance spectroscopy (PEIS), cyclic voltammetry (CV) and galvanostatic cycling with potential limitation (GCPL) were performed in a thermostatically controlled chamber to avoid temperature oscillations.

Two-electrode potentiostatic electrochemical impedance (PEIS) measurements were acquired during the 1st, 25th and 50th cycle, either upon galvanostatic cycling (bias potential $E = 3.4$ V) or cyclic voltammetry at the discharged state ($E = 2.5$ V). For all EIS measurements, a sinusoidal perturbation with $\Delta E = \pm 5$ mV was applied over the frequency range 100 mHz $< f <$ 200 kHz, with 6 points per decade and logarithmic spacing. The obtained Nyquist plots were fitted by the Equivalent Circuit Method (ECM) through a non-linear least-squares (NLLS) protocol,[43,44] using the software *RelaxIS3*. In order to guarantee the goodness of the fitting procedure, only fitted functions with $\chi^2 < 1\times10^{-4}$ were considered acceptable.

The electrochemical stability of the GPE and liquid electrolyte was investigated by sodium stripping and plating tests on a Na/ electrolyte/ Na symmetric cell for over 50 cycles.

The electrochemical stability window of the membrane was studied through cyclic voltammetry (CV) in the cathodic region and linear sweep voltammetry (LSV) in the anodic region. For this type of experiment, the working electrode (WE) was produced by mixing conductive carbon (P45) and PVDF (8:2) in NMP and then casting the so obtained slurry onto aluminium and copper current collectors. The cell configuration used was Na/ electrolyte/ WE.

The ionic conductivity of the GPE and liquid electrolytes was determined by impedance spectroscopy in the 101 kHz–5 mHz frequency range using a custom Teflon O-ring (16 mm external diameter and 9 mm internal diameter) and stainless steel (SS) as blocking electrode in a SS/ electrolyte/ SS cell configuration. For this purpose, impedance spectra have been acquired in a temperature range between 5 °C–55 °C with T steps of 5 °C. For the calculation of σ, the following equation was applied:

$$\sigma = \frac{L}{RA}$$

where L is the thickness of the membrane, R is the bulk resistance obtained from impedance measurement and A is the surface contact area. The activation energy was calculated by means of the following equation:

$$E_a = -R \times Slope$$

Where E_a is the activation energy, R is the gas constant, and the Slope was obtained by the linear fit of the Arrhenius plot.

The Li^+ transference number of the GPE was found applying the Bruce-Vincent-Evans method:

$$\tau^+ = \frac{i_{ss}}{i_0} \times \frac{(\Delta V - R_0 i_0)}{(\Delta V - R_{ss} i_{ss})}$$

A symmetrical cell made of Na/ electrolyte/ Na was assembled and tested at three different temperatures (15 °C, 25 °C and 35 °C). For the chronoamperometric measurements, a voltage of 30 mV was applied for 60 min and the impedance spectra were recorded at the initial and steady state cell polarization in the 101 kHz–5 mHz frequency range.

The diffusion coefficient of the two cathodes was determined using both the liquid and the gel electrolyte. Before acquiring CV at different scan rates (0.1 $mV s^{-1}$, 0.15 $mV s^{-1}$, 0.2 $mV s^{-1}$, 0.25 $mV s^{-1}$ and 0.3 $mV s^{-1}$), the cell was cycled 2 times at C/10 in order to ensure a stable capacity and the formation of a passivation layer. The Randles-Sevcik equation was applied for D calculation:

$$ip = 0.4463\ n\ FAC\ \sqrt{\frac{FDv}{RT}}$$

Where: I_p = scan rate current, n = number of electrons transferred in the process, A = area off the electrode, F=Faraday constant, D = diffusion coefficient, C = concentration, v = scan rate, R = gas constant, T = temperature.

The galvanostatic charge discharge profiles were acquired within the 2.5–4.3 V voltage range applying a current density corresponding to C/10 (1 C = 170 $mAh g^{-1}$) at 25 °C. For PBs characterization, the 9 mm electrode (0.636 cm^2 surface area) was tested in CR2032 coin cell using conventional $NaClO_4$ 1 M in EC:PC (1:1 v/v) liquid electrolyte and sodium as negative electrode.

All the potential values are referred to the Na^+/Na redox couple ($E° = -2.71$ V vs. RHE).

X-Ray Photoelectron Spectroscopy (XPS) analyses were conducted using a PHI 5000 VersaProbe instrument from ULVAC-PHI (Physical Electronics Inc., Kanagawa, Japan). The instrument utilized monochromatic Al Kα radiation with an energy of 1486.6 eV as the X-ray source. Two distinct pass energy values were applied, with 187.75 eV for the survey spectra and 23.5 eV for the high-resolution (HR) spectra.

Acknowledgements

The authors thank HP Composites and the Italian Ministry of University and Research for funding the doctoral fellowship of A.P. in the framework of the project "Composite Materials Hub of Valle del Tronto, Marche region". The authors acknowledge the financial support of the University of Camerino through the FAR 2022 PNR program: NAMMOF project. Part of this research was carried out in the framework of the collaboration agreement with ENEA (Agenzia Nazionale per le Nuove Technologie, l'Energia e lo Sviluppo Sostenibile) and MiTE (Ministero della Transizione Ecologica) "Integrated project for electrochemical and thermal storage technologies"–PTR Program 2022–2024. Open Access publishing facilitated by Università degli Studi di Camerino, as part of the Wiley - CRUI-CARE agreement.

Conflict of Interests

The authors declare no conflict of interest.

Data Availability Statement

The data that support the findings of this study are available from the corresponding author upon reasonable request.

Keywords: Na-ion battery · Solid-state battery · Prussian blue analogues · Metal-organic frameworks · Gel polymer electrolyte

[1] J. I. Kim, et al., *Adv. Funct. Mater.* **2017**, *27*, 1701768. DOI: 10.1002/adfm.201701768.
[2] J. Zheng, et al., *Energy and Environmental Materials.* **2023**, *6*, e12422. DOI: 10.1002/eem2.12422.
[3] G. Xi, et al., *Adv. Funct. Mater.* **2021**, *31*, 2007598. DOI: 10.1002/adfm.202007598.
[4] V. Marangon, et al., *J. Power Sources* **2020**, *449*, 227508. DOI: 10.1016/j.jpowsour.2019.227508.
[5] V. Marangon, et al., *Chem. Eur. J.* **2023**, *29*, e202301345. DOI: 10.1002/chem.202301345.
[6] B. Scrosati, J. Garche, *J. Power Sources* **2010**, *195*, 2419. DOI: 10.1016/j.jpowsour.2009.11.048.
[7] A. Patriarchi, et al., *Batteries.* **2024**, *10*, 11. DOI: 10.3390/batteries10010011.
[8] J. I. Kim, et al., *J. Membr. Sci.* **2018**, *566*, 122.DOI: 10.1016/j.memsci.2018.08.066.
[9] K. M. Winslow, et al., *Resour. Conserv. Recycl.* **2018**, *129*, 263. DOI: 10.1016/j.resconrec.2017.11.001.
[10] D. B. Agusdinata, et al., *Environ. Res. Lett.* **2018**, *13*, 123001. DOI: 10.1088/1748-9326/aae9b1.

[11] H. Gao, et al., *Adv. Energy Mater.* **2016**, *6*, 1600467. DOI: 10.1002/aenm.201600467.
[12] M. Chen, et al., *Nat. Commun.* **2019**, *10*, 1480. DOI: 10.1038/s41467-019-09170-5.
[13] J. Billaud, et al., *J. Am. Chem. Soc.* **2014**, *136*, 17243. DOI: 10.1021/ja509704t.
[14] J. Peng, et al., *Adv. Mater.* **2022**, *34*, 2108384. DOI: 10.1002/adma.202108384.
[15] Y. Matos-Peralta, M. Antuch, *J. Electrochem. Soc.* **2020**, *167*, 2108384. DOI: 10.1149/2.0102003jes.
[16] Y. Yang, et al., *Nano Energy* **2022**, *99*, 107424. DOI: 10.1016/j.nanoen.2022.107424.
[17] Y. Chen, et al., *ACS Appl. Nano Mater.* **2022**, *5*, 4833. DOI: 10.1021/acsanm.1c04416.
[18] J. Qian, et al., *Adv. Energy Mater.* **2018**, *8*, 1702619. DOI: 10.1002/aenm.201702619.
[19] K. Xu, *Chem. Rev.* **2014**, *114*, 11503. DOI: 10.1021/cr500003w.
[20] X. Cheng, et al., *Adv. Energy Mater.* **2018**, *8*, 1702184. DOI: 10.1002/aenm.201702184.
[21] Y. You, et al., *Energy Environ. Sci.* **2014**, *7*, 1643. DOI: 10.1039/c3ee44004d.
[22] W. J. Li, et al., *Small.* **2019**, *15*, 1900470. DOI: 10.1002/smll.201900470.
[23] F. Herren, et al., *Inorg. Chem.* **1980**, *19*, 956. DOI: 10.1021/ic50206a032.
[24] W. Wang, et al., *Nat. Commun.* **2020**, *11*, 980. DOI: 10.1038/s41467-020-14444-4.
[25] A. Zhou, et al., *Adv. Energy Mater.* **2021**, *11*, 2000943. DOI: 10.1002/aenm.202000943.
[26] P. Bhatt, et al., *Phys. Rev. B* **2023**, *108*, 014412. DOI: 10.1103/PhysRevB.108.014412.
[27] C. Yan, et al., *Electrochim. Acta* **2020**, *332*, 135533. DOI: 10.1016/j.electacta.2019.135533.
[28] D. Seyferth, *J. Organomet. Chem.* **1978**, *7*, 2163. DOI: 10.1016/s0022-328x(00)93553-8.
[29] S. F. A. Kettle, et al., *Inorg. Chem.* **2007**, *46*, 2409. DOI: 10.1021/ic0610482.
[30] R. Mažeikien, et al., *J. Electroanal. Chem.* **2011**, *660*, 140. DOI: 10.1016/j.jelechem.2011.06.022.
[31] G. Moretti, C. Gervais, *J. Raman Spectrosc.* **2018**, *49*, 1198. DOI: 10.1002/jrs.5366.
[32] M. Youssry, et al., *RSC Adv.* **2018**, *8*, 32119. DOI: 10.1039/c8ra05446k.
[33] J. Sun, et al., *Energy Storage Mater.* **2021**, *43*, 182. DOI: 10.1016/j.ensm.2021.09.004.
[34] H. Sun, et al., *RSC Adv.* **2014**, *4*, 42991. DOI: 10.1039/c4ra07531e.
[35] X. Wu, et al. *Electrochem. Commun.* **2013**, *31*, 145. DOI: 10.1016/j.elecom.2013.03.013.
[36] J. Zhang, et al., *Particuology.* **2022**, *61*, 18. DOI: 10.1016/j.partic.2021.05.006.
[37] Y. Huang, et al., *Nano Energy* **2017**, *39*, 273. DOI: 10.1016/j.nanoen.2017.07.005.
[38] X. Yan, et al., *Electrochim. Acta* **2017**, *225*, 235. DOI: 10.1016/j.electacta.2016.12.121.
[39] M. Zarrabeitia, et al., *Batteries.* **2017**, *3*, 16. DOI: 10.3390/batteries3020016.
[40] J. E. B. Randles, *Faraday Discuss.* **1947**, *1*, 11. DOI: 10.1039/DF9470100011.
[41] F. Maroni, et al., *ChemElectroChem.* **2023**, *10*, e202201070. DOI: 10.1002/celc.202201070.
[42] L. Li, et al., *J. Mater. Chem. A* **2019**, *7*, 12134. DOI: 10.1039/c9ta01965k.
[43] B. A. Boukamp, *Solid State Ionics* **1986**, *18–19*, 136. DOI: 10.1016/0167-2738(86)90100-1.
[44] B. A. Boukamp, *Solid State Ionics* **1986**, *20*, 31. DOI: 10.1016/0167-2738(86)90031-7.
[45] I. D. Raistricket, *Impedance Spectroscopy - Theory, Experiment, and Applications*, Wiley **2005**, pages 80–117 .
[46] B. Kang, G. Ceder, *Nature* **2009**, *458*, 190. DOI: 10.1038/nature07853.
[47] D. J. Lin, et al., *Eur. Polym. J.* **2006**, *42*, 2407. DOI: 10.1016/j.eurpolymj.2006.05.008.
[48] W. Pu, et al., *J. Membr. Sci.* **2006**, *280*, 6. DOI: 10.1016/j.memsci.2006.05.028.
[49] J. Xi, et al., *J. Power Sources* **2006**, *157*, 501. DOI: 10.1016/j.jpowsour.2005.08.009.
[50] F. Deng, et al., *J. Membr. Sci.* **2015**, *491*, 82. DOI: 10.1016/j.memsci.2015.05.021.
[51] Q. Xiao, et al., *J. Membr. Sci.* **2009**, *334*, 117. DOI: 10.1016/j.memsci.2009.02.018.
[52] I. S. Elashmawi, L. H. Gaabour, *Results Phys.* **2015**, *5*, 105. DOI: 10.1016/j.rinp.2015.04.005.
[53] H. Yu, et al., *ACS Omega* **2021**, *6*, 29060. DOI: 10.1021/acsomega.1c04275.
[54] S. Liang, et al., *ChemElectroChem.* **2019**, *6*, 5413. DOI: 10.1002/celc.201901351.
[55] J. Maxfield, I. W. Shepherd, *Polymer* **1975**, *16*, 505. DOI: 10.1016/0032-3861(75)90008-7.
[56] I. Rey, et al. *J. Electrochem. Soc.* **1998**, *145*, 3034. DOI: 10.1149/1.1838759.
[57] P. R. Griffiths, *Vib. Spectrosc.* **1992**, *4*, 121. DOI: 10.1016/0924-2031(92)-87021-7.
[58] I. Rey, et al. *Electrochim. Acta* **1998**, *43*, 1505. DOI: 10.1016/S0013-4686(97)10092-5.
[59] R. Prasanth, et al., *J. Power Sources* **2014**, *24*, 5283.DOI: 10.1016/j.jpowsour.2013.05.178.
[60] M. Basappa, et al., *Chem. Phys. Lett.* **2022**, *799*, 139609. DOI: 10.1016/j.cplett.2022.139609.
[61] S. Das, A. Ghosh, *J. Appl. Phys.* **2016**, *119*, 95101. DOI: 10.1063/1.4942658.
[62] P. De Sainte Claire, *Macromolecules.* **2009**, *42*, 3469. DOI: 10.1021/ma802469u.
[63] J. W.Choi, et al., *Journal of Industrial and Engineering Chemistry.* **2006**, *12*, 939.
[64] X. Li, et al., *J. Power Sources* **2007**, *167*, 491. DOI: 10.1016/j.jpowsour.2007.02.032.
[65] Barsoukov, E. Macdonald, J. R. *Impedance Spectroscopy: Theory, Experiment, and Applications* **2005**, pages 424-458 .
[66] J. Castillo, et al., *Chem. Mater.* **2021**, *33*, 8812. DOI: 10.1021/acs.chemmater.1c02952.
[67] S. S. Zhang, et al. *J. Power Sources* **2004**, *125*, 114. DOI: 10.1016/j.jpowsour.2003.07.008.
[68] J. Y. Song, et al. *J. Electrochem. Soc.* **2002**, *149*, A1230. DOI: 10.1149/1.1499963.
[69] M. Menisha, et al., *Solid State Ionics* **2021**, *37*, 1115755. DOI: 10.1016/j.ssi.2021.115755.
[70] S. Janakiraman, et al., *Solid State Ionics* **2016**, *104*, 130. DOI: 10.1016/j.ssi.2016.05.020.
[71] K. Xu, *Chem. Rev.* **2004**, *104*, 4303. DOI: 10.1021/cr030203g.
[72] S. A. Suthanthiraraj, M. K. Vadivel, *Appl. Nanosci.* **2012**, *2*, 239. DOI: 10.1007/s13204-012-0099-3.
[73] V. M. Mohan, et al., *J. Polym. Res.* **2007**, *14*, 283. DOI: 10.1007/s10965-007-9108-8.
[74] S. B. Aziz, et al., *J. Sci. Adv. Mater. Devices* **2018**, *3*, 1. DOI: 10.1016/j.jsamd.2018.01.002.
[75] I. J. A. Mertens, et al., *Macromolecules.* **1999**, *32*, 3314. DOI: 10.1021/ma981901j.
[76] Y. Zhou, et al., *Electrochim. Acta* **2019**, *324*, 134827, DOI: 10.1016/j.electacta.2019.134827.
[77] H. Verma, et al., *J. Solid State Electrochem.* **2020**, *24*, 521. DOI: 10.1007/s10008-019-04490-4.
[78] V. K. Singh, et al., *J. Solid State Electrochem.* **2018**, *22*, 1909. DOI: 10.1007/s10008-018-3891-5.
[79] D. Kumar, *Solid State Ionics* **2018**, *318*, 65. DOI: 10.1016/j.ssi.2017.09.006.
[80] I. van der Veen, J. de Boer, *Chemosphere.* **2012**, *88*, 1119.DOI: 10.1016/j.chemosphere.2012.03.067.
[81] A. Granzow, *Acc. Chem. Res.* **1978**, *11*, 177. DOI: 10.1021/ar50125a001.
[82] D. Price, et al., *Polym. Degrad. Stab.* **2007**, *92*, 1101. DOI: 10.1016/j.polymdegradstab.2007.02.003.
[83] J. Guo, et al., *Chem. Eng. J.* **2021**, *422*, 130526 DOI: 10.1016/j.cej.2021.130526.
[84] G. T. K. Fey, et al., *J. Power Sources* **2009**, *189*, 169. DOI: 10.1016/j.jpowsour.2008.10.016.
[85] A. S. Aricò, et al., *Nat. Mater.* **2005**, *4*, 366. DOI: 10.1038/nmat1368.
[86] F. Hasan, et al., *Journal of Electrochemical Science and Technology.* **2020**, *11*, 00899. DOI: 10.33961/jecst.2020.00899.
[87] T. V. S. L. Satyavani, et al., *Engineering Science and Technology, an International Journal.* **2016**, *19*, 40. DOI: 10.1016/j.jestch.2015.05.011.
[88] S. Y. Chung, et al. *Nat. Mater.* **2002**, *1*, 123. DOI: 10.1038/nmat732.
[89] N. J. Dudney, J. Li, *Science* **2015**, *347*, 131. DOI: 10.1126/science.aaa2870.
[90] W. J. Zhang, *J. Power Sources* **2011**, *196*, 2962. DOI: 10.1016/j.jpowsour.2010.11.113.

[91] W. Wang, et al., *Adv. Funct. Mater.* **2022**, *32*, 2111727. DOI: 10.1002/adfm.202111727.
[92] Y. Jiang, et al., *Adv. Funct. Mater.* **2016**, *26*, 1600747. DOI: 10.1002/adfm.201600747.
[93] S. P. Kühn, et al., *Adv. Mater. Interfaces* **2022**, *9*, 2102078. DOI: 10.1002/admi.202102078.
[94] Y. Huang, et al., *Adv. Mater.* **2019**, *31*, 1808393. DOI: 10.1002/adma.201808393.
[95] W. Fu, et al., *J. Power Sources* **2023**, *561*, 232738. DOI: 10.1016/j.jpowsour.2023.232738.
[96] M. Gauthier, et al. *J. Phys. Chem. Lett.* **2015**, *6*, 4653. DOI: 10.1021/acs.jpclett.5b01727.
[97] M. Ye, et al., *Mater. Today Energy* **2022**, *23*, 21100898. DOI: 10.1016/j.mtener.2021.100898.
[98] P. Bhatt, et al., *New J. Chem.* **2018**, *42*, 4567. DOI: 10.1039/c8nj00451j.
[99] J. Song, et al., *Adv. Energy Mater.* **2018**, *8*, 1703082. DOI: 10.1002/aenm.201703082.
[100] I. Moeez, et al., *Chem. Eng. J.* **2021**, *425*, 21130547. DOI: 10.1016/j.cej.2021.130547.
[101] R. Raccichini, et al., *Batteries.* **2019**, *5*, 12. DOI: 10.3390/batteries5010012.
[102] P. Vadhva, et al., *ChemElectroChem.* **2021**, *8*, 1930. DOI: 10.1002/celc.202100108.
[103] A. C. Lazanas, M. I. Prodromidis, *ACS Measurement Science Au.* **2023**, *3*, 162, DOI: 10.1021/acsmeasuresciau.2c00070.
[104] P. Bhatt, et al., *New J. Chem.* **2018**, *42*, 4567. DOI: 10.1039/c8nj00451j.
[105] M. Xie, et al., *ChemElectroChem.* **2019**, *6*, 2423, DOI: 10.1002/celc.201900101.
[106] M. Xu, et al., *Energy Storage Mater.* **2022**, *44*, 477. DOI: 10.1016/j.ensm.2021.10.038.
[107] J. Rodríguez-Carvajal, *Physica B: Physics of Condensed Matter.* **1993**, *192*, 55. DOI: 10.1016/0921-4526(93)90108-I.
[108] T. Roisnel, J. Rodríguez-Carvajal, *Mater. Sci. Forum* **2001**, *378*, 118. DOI: 10.4028/www.scientific.net/msf.378-381.118.
[109] A. Altomare, et al. *J. Appl. Crystallogr.* **2013**, *46*(4), 1231. DOI: 10.1107/S0021889813013113.
[110] B. H. Toby, R. B. Von Dreele, *J. Appl. Crystallogr.* **2013**, *46*, 544. DOI: 10.1107/S0021889813003531.

Manuscript received: November 4, 2024
Version of record online: January 16, 2025